

Raman mapping of photodissociation regions

William J. Henney^{ID}[★]

Instituto de Radioastronomía y Astrofísica, Universidad Nacional Autónoma de México, Apartado Postal 3-72, 58090 Morelia, Michoacán, Mexico

Accepted 2021 January 25. Received 2021 January 24; in original form 2020 December 27

ABSTRACT

BroadRaman-scattered wings of hydrogen lines can be used to map neutral gas illuminated by high-mass stars in star-forming regions. Raman scattering transforms far-ultraviolet starlight from the wings of the Ly β line (1022–1029 Å) to red visual light in the wings of the H α line (6400–6700 Å). Analysis of spatially resolved spectra of the Orion Bar and other regions in the Orion Nebula shows that this process occurs in the neutral photodissociation region between the ionization front and dissociation front. The inner Raman wings are optically thick and allow the neutral hydrogen density to be determined, implying $n(\text{H}^0) \approx 10^5 \text{ cm}^{-3}$ for the Orion Bar. Far-ultraviolet resonance lines of neutral oxygen imprint their absorption on to the stellar continuum as it passes through the ionization front, producing characteristic absorption lines at 6633 Å and 6664 Å with widths of order 2 Å. This is a unique signature of Raman scattering, which allows it to be easily distinguished from other processes that might produce broad H α wings, such as electron scattering or high-velocity outflows.

Key words: radiative transfer – atomic physics – ISM: individual objects (Orion Nebula) – photodissociation regions.

1 INTRODUCTION

Raman scattering is the inelastic analogue of Rayleigh scattering by atoms or molecules. Both processes begin with a radiation-induced transition of an electron to a virtual bound state (non-eigenstate). In Rayleigh scattering, the electron returns to its original state, resulting in the radiation being re-emitted with its original frequency (elastic scattering). In Raman scattering, on the other hand, the electron undergoes a transition to a different excited state, resulting in radiation being re-emitted at a much lower frequency. See Fig. 1 for an illustration of the process. Recently, Dopita et al. (2016) identified exceedingly broad wings to the H α 6563 Å line in the Orion Nebula and a number of H II regions in the Magellanic Clouds, which they ascribe to Raman scattering of ultraviolet radiation in the vicinity of the Ly β 1025 Å transition. Raman scattering in astrophysical sources was first identified in symbiotic stars (Schmid 1989), where FUV O VI emission lines at 1032 and 1038 Å produce broad emission features at 6827 and 7088 Å. This illustrates a curious feature of Raman scattering (Nussbaumer, Schmid & Vogel 1989): the relative width $\Delta\lambda/\lambda$ of spectral features is amplified by a factor $\lambda(\text{H}\alpha)/\lambda(\text{Ly}\beta) \approx 6.4$ when passing from the FUV to the optical domain. Further astrophysical applications have included planetary nebulae (Pequignot et al. 1997; Arrieta & Torres-Peimbert 2003; Lee et al. 2006) and active galactic nuclei (Chang et al. 2015).

Dopita et al. (2016) propose that the Raman wings form at the transition zone near the ionization fronts in H II regions. However, the total neutral hydrogen column through the ionization front can be no more than about $10/\sigma_0 \approx 2 \times 10^{18} \text{ cm}^{-2}$, where $\sigma_0 \approx 6.3 \times 10^{-18} \text{ cm}^2$ is the ground-state hydrogen photoionization cross-section at the Lyman limit (Osterbrock & Ferland 2006). The Raman-scattering cross-section at wavelengths responsible for the observed wings is much lower than this: $\sigma_{\text{Raman}} \sim 10^{-21} \text{ cm}^2$

(Chang et al. 2015), meaning that the Raman-scattering optical depth through the ionization front is only of order 0.001. A vastly larger column density of neutral hydrogen ($\approx 10^{21} \text{ cm}^{-2}$) is available in the photodissociation region (PDR) outside the ionization front, so it is more likely that Raman scattering will occur there instead, so long as there is sufficient far-ultraviolet radiative flux.

This paper is organized as follows. Section 2 presents archival VLT-MUSE integral field spectroscopy of the Orion Nebula. Spectra of the broad H α wings are extracted for key areas of the nebula (Section 2.1). Two components of the O I UV resonance multiplet $2s2p^4 {}^3P \rightarrow 2s2p^3 {}^3d {}^3D^0$ are detected as absorption features at 6633 and 6664 Å against the H α Raman wings (Section 2.2). Three wavelength bands are defined in each of the red and blue wings that avoid contaminating emission and absorption features (Section 2.3). The emission bands are spatially mapped and compared with other tracers of ionized and neutral zones in the nebula (Section 2.4). Particular attention is paid to the edge-on PDR at the Orion Bar (Section 2.5). Equivalent widths of the Raman-scattered absorption lines are compared with the distribution of other absorption features in the nebula (Section 2.6). Section 3 presents archival Keck-HIRES slit spectroscopy, which shows the profile of the 6664 Å absorption line with an effective velocity resolution of 1 km s^{-1} . Section 4 discusses the implications of these results for the structure of the PDRs in Orion. An appendix recapitulates the basic theory of Raman scattering, concentrating on the wavelength transformation from the FUV domain around Ly β to optical domain around H α . In addition, polynomial fits are provided to the wavelength dependence of the total (Rayleigh plus Raman) scattering cross-section and the Raman H α branching ratio.

2 SPECTRAL MAPPING OF RAMAN WINGS

The principal observational data set used in this paper is the imaging spectroscopy mosaic of the inner Orion Nebula (Weilbacher et al. 2015; Mc Leod et al. 2016) obtained with the MUSE spectrograph

* E-mail: w.henney@irya.unam.mx

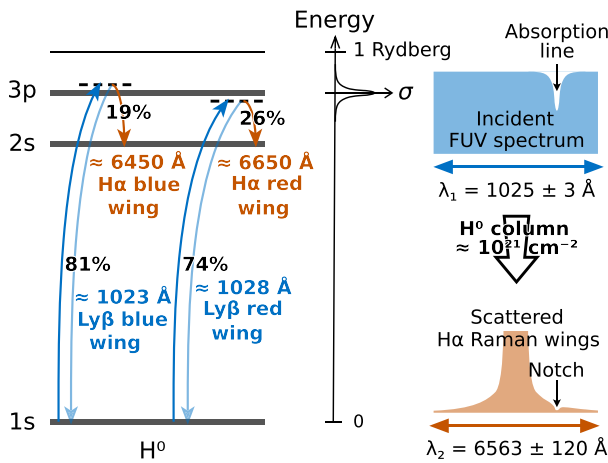


Figure 1. Schematic illustration of Raman scattering of photons from the H α wings to the H α wings. The relevant energy levels of neutral hydrogen are shown at left. Far ultraviolet photons that are shifted by about $\Delta\lambda_1 = \pm 1$ to 3 Å from the Ly β rest wavelength can excite transitions from the ground 1-s level to a virtual state adjacent to 3p. Most such excitations decay back to 1s (Rayleigh scattering), but in about one-fifth of cases, the decay is to 2s instead (Raman scattering). The scattering cross-section falls approximately as $\Delta\lambda_1^{-2}$, which gives broad Lorentzian wings to the H α line, as shown at right. A bandwidth of $\Delta\lambda_1 = \pm 3$ Å around Ly β is transformed to a bandwidth $\Delta\lambda_2 \approx \pm 120$ Å around H α . A narrow absorption line in the incident FUV spectrum (vertical thin dashed line) becomes a much broader notch in the scattered wings.

(Bacon et al. 2010, 2014) on the VLT. The entire data cube covers the wavelength range 4595–9366 Å but we concentrate mainly on the range 6300–6800 Å, where the spectral resolving power is $R \approx 2500$, corresponding to an instrumental linewidth [full width at half-maximum (FWHM)] of $\delta\lambda \approx 2.4$ Å, which is sampled at 1.25 Å pixel $^{-1}$ and then resampled to 0.85 Å pixel $^{-1}$ for the final calibrated cube (see section 2 of Weilbacher et al. 2015). The observed field is shown by the white rectangle in Fig. 2(a) and includes the entire inner Huygens region of the nebula, which accounts for roughly half of the total radio continuum flux from the H II region (Subrahmanyan, Goss & Malin 2001). The full data cube is a mosaic that combines observations from 30 separate pointings, with a pixel size of $0.2 \times 0.2''$.

2.1 Raman-scattered H α wings

Extended wings to the H α line are detected over the entire map, but they are particularly prominent in the six regions marked as white boxes in Fig. 2(b). These are all bar-like features (O'Dell & Yusef-Zadeh 2000; García-Díaz & Henney 2007), which correspond to filamentary ionization fronts. Extracted MUSE spectra around the H α line for each of these regions are shown in Fig. 3. All regions show broad wings to the H α line extending from 6300 to 6700 Å, which are consistent with the higher spectral resolution ($R = 7000$) results of Dopita et al. (2016) for the region indicated by a dashed box in Fig. 2(b). Two additional extraction regions (dotted boxes in the figure) are chosen to cover the blueshifted high-ionization ‘Big Arc’ feature (Doi, O'Dell & Hartigan 2004), where the extended wings are relatively weak, and the highly extinguished ‘Dark Bay’ to the NE of the nebula. The continuum is interpolated under the wings by fitting a second-order polynomial to clean regions of the spectra in the ranges 6070–6225 Å and 6760–Å, as shown by the lower edge of the grey shading for each spectrum. The continuum is mostly a combination

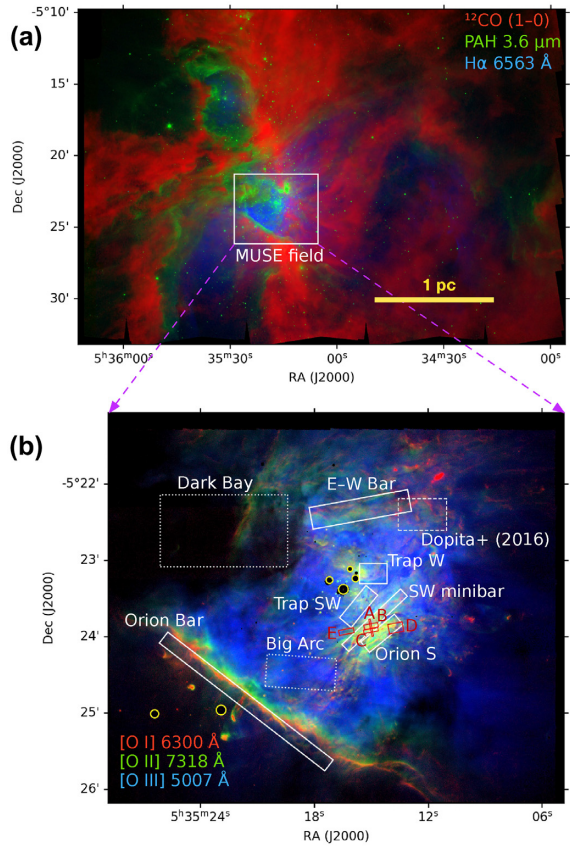


Figure 2. (a) Panoramic view of the Orion Nebula region on parsec scales. Red channel of background image shows ^{12}CO (1-0) emission from dense molecular gas (Carma-NRO Orion Survey, Kong et al. 2018). Green channel shows near-infrared continuum from PAH grains in neutral gas (Spitzer Orion Survey, Megeath et al. 2012). Blue channel shows optical H α emission from ionized gas (WFI camera on ESO 2.2 m La Silla, Da Rio et al. 2009). The white box shows the field of view observed with MUSE. (b) Locations within the nebula of the extraction regions for the MUSE spectra shown in Fig. 3 (white boxes) and the Keck HIRES spectra shown in Fig. 11 (red boxes). The region of the spectrum obtained in Dopita et al. (2016) is shown by the dashed box. Background image shows oxygen emission lines extracted from the MUSE data cube: [O I] $\lambda 6300$ Å (red channel), which traces ionization fronts and shocks in neutral gas; [O II] $\lambda 7318$ Å (green channel), which traces the outer layers of the photoionized nebula; and [O III] $\lambda 5007$ Å (blue channel), which traces the highly ionized interior of the nebula.

of Paschen recombination emission from hydrogen, which increases to the red, and dust-scattered starlight and two-photon hydrogen emission, which both increase to the blue. The combined F_λ is approximately flat for all regions except the Orion Bar, where dust scattering of the nearby star θ^2 Ori A dominates, resulting in a blueward rise. All of these continuum processes are expected to be smooth on a 100 Å scale,¹ but none the less, the systematic uncertainties in the continuum interpolation is an important factor that limits the precision of the Raman wing measurements.

Another potential contribution to the continuum comes from Extended Red Emission (ERE; Schmidt, Cohen & Margon 1980),

¹One exception is the dust-scattered H α line from the stellar photospheres and winds, but this is confined within ± 30 Å of the rest wavelength (see fig. 2 of Simón-Díaz et al. 2006) and so does not affect the Raman wings, which are broader than that.

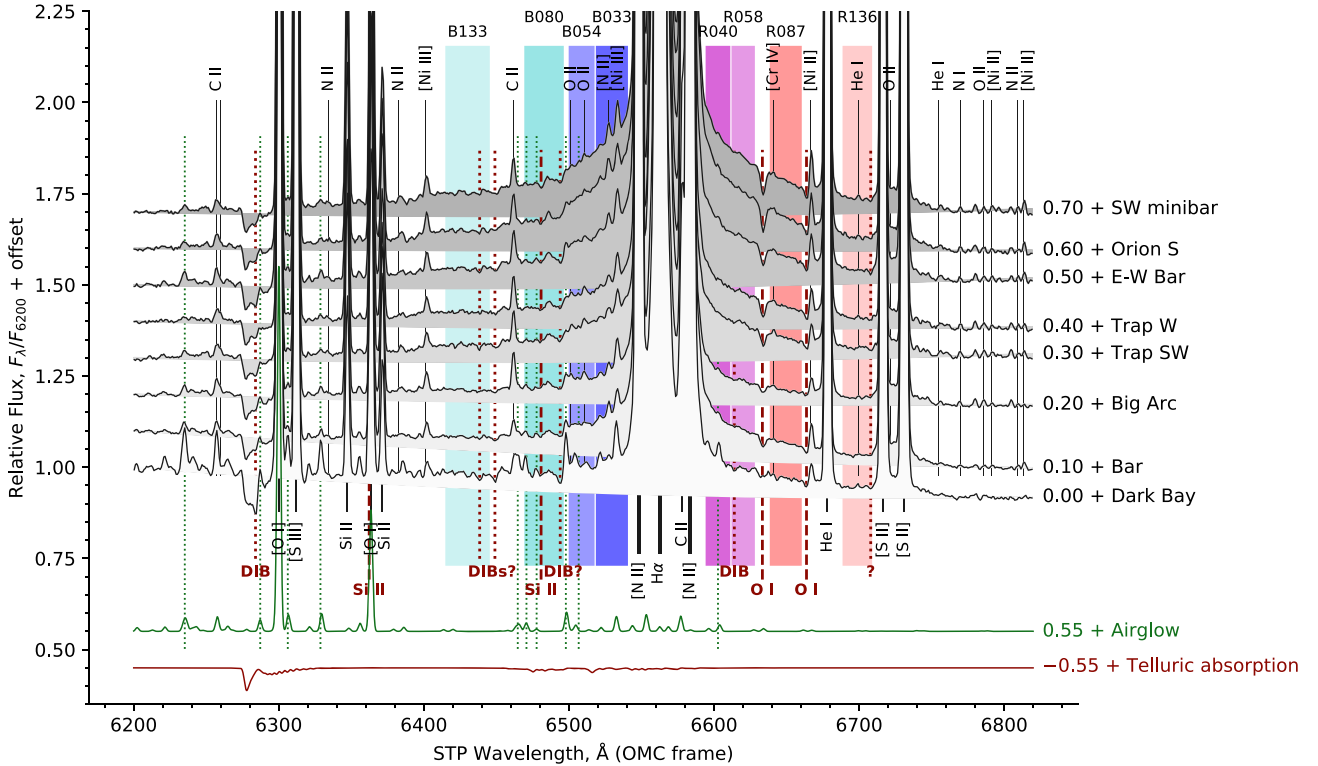


Figure 3. MUSE spectra of the Orion Nebula centred on the $\text{H}\alpha$ line, showing the broad Raman-scattered wings. Spectra are shown for the regions outlined by white boxes in Fig. 2 and were extracted from the data cubes of Weilbacher et al. (2015). All spectra are normalized to the continuum at 6200 Å and are offset vertically as labelled at right. Emission line identifications are shown by solid vertical lines, labelled above for weak lines and below for stronger lines. Wavelengths of Raman-scattered O I and Si II absorption lines from Table A1 are shown by red dashed vertical lines, labelled in bold font below, together with candidate DIB and unidentified absorption features marked with '?'. Dotted lines show night sky lines identified in the Dark Bay region of the nebula. At the bottom of the figure are shown the theoretical upper-atmosphere airglow spectrum (green line) and telluric molecular absorption spectrum (red line), as calculated from the Cerro Paranal Advanced Sky Model (Noll et al. 2012; Moehler et al. 2014).

which is likely to be the result of complex fluorescent processes in small carbon-based molecules (Witt & Lai 2020) that are located in the neutral hydrogen region (Lai, Witt & Crawford 2017). A broad bump ($\text{FWHM} \approx 1800$ Å) centred on ≈ 8200 Å is reported in the spectrum of sections of the Orion Bar by Perrin & Sivan (1992). This ERE may conceivably have sub-structure that affects the extraction of the Raman wing intensities.

2.2 Raman-scattered FUV absorption lines

A prominent feature of all the spectra in Fig. 3 is a pair of absorption notches in the red wing at 6633 Å and 6664 Å, which closely correspond to the wavelengths expected for the Raman-scattered transformation of the O I resonance lines at 1027 Å and 1028 Å listed in Table A1. After correcting for instrumental broadening, the FWHM of the 6633 Å feature is ≈ 2.5 Å, which would correspond to a velocity width of 115 km s^{-1} if it were an optical absorption line. However, taking into account the wavelength transformation during Raman scattering (equation A2), the true velocity width of the FUV line is 18 km s^{-1} . The absorption depth of the features is roughly 50 per cent with respect to the Raman-scattered wing at adjacent wavelengths but is much less than this with respect to the total continuum emission. The same spectral features are also visible in the Dopita et al. (2016) spectra but are not commented on by those authors. The 6664 Å feature is partially blended with the [Ni II] 6666.8 Å nebular emission line in the MUSE spectra, but these are

better resolved in the higher resolution Dopita et al. spectra. Archival Keck HIRES observations of this feature at an even higher spectral resolution are presented below in Section 3. The identification of these two FUV absorption lines in the optical spectrum is uncontested proof of a Raman-scattering origin for the broad $\text{H}\alpha$ wings.

There is also evidence for a weak absorption feature in the blue wing at 6481 Å, corresponding to the Si II absorption line at 1024 Å. However, the blue wing is much less clean than the red wing, partly due to telluric absorption and airglow emission (see below), which makes the identification uncertain. The Raman wings show some other weak features of uncertain origin, the strongest of which is an apparent broad (≈ 5 Å) absorption feature at 6494 Å, while additional narrower features are seen at 6439, 6449, and 6708 Å (all marked in Fig. 3). It is likely that at least some of these features may be Diffuse Interstellar Bands (DIBs) (see Section 2.6.3 below), as evidenced by their correlation with foreground dust extinction (they are strongest in the Dark Bay sample, where the extinction is highest). Two definite DIB features are seen at 6284 Å (strong, but superimposed on telluric absorption) and 6614 Å (weak).

2.3 Definition of observational Raman bands in the red and blue wings

In order to study the spatial distribution of the Raman-scattered wings, it is convenient to define a series of broad bands on the blue and red sides, which are listed in Table 1 and shown as blue- and

Table 1. Wavelength bands used for Raman wing extraction.

	Band (1)	$(\Delta\lambda_2)$, Å (2)	λ_{min} , Å (3)	λ_{max} , Å (4)	$f_{\text{H}\alpha}$ (5)	$\langle\sigma_\lambda\rangle$, 10^{-21} cm^2 (6)	Contamination (7)
Blue wing	B133	−132.8	6414.85	6445.45	0.180	0.144	
	B080	−79.5	6469.25	6496.45	0.196	0.378	Sky 6471, 6478, H ₂ O
	B054	−53.6	6499.85	6517.70	0.205	0.802	O II? 6502, 6510, Sky 6507, H ₂ O
	B033	−32.8	6518.55	6540.65	0.212	2.069	[N II] 6527.24, [Ni III] 6533.76, H ₂ O
Red wing	R040	40.3	6594.20	6611.20	0.238	1.451	Sky 6603
	R058	57.7	6612.05	6628.20	0.244	0.695	
	R087	87.1	6638.40	6660.50	0.255	0.299	[Cr IV]? 6641
	R136	135.7	6688.55	6708.95	0.274	0.119	He I 6699

Note. COLUMNS: (1) Name of band. (2) Mean wavelength displacement from H α rest wavelength. (3, 4) Upper and lower wavelength limits for the band. (5) Mean value of the H α branching ratio from virtual 3p levels [see equation (A6)]. (6) Mean value of Ly β wing cross-section that can feed this band via Raman scattering [see equation (A5)]. (7) Nebular and telluric lines that may contaminate the band (see text for details).

red-shaded vertical stripes in Fig. 3. Four bands are defined in each wing, spanning a range in $|\Delta\lambda_2|$ from about 30 Å to 150 Å. The lower limit of this range is determined by overlap with the strong nebular [N II] emission lines, while the upper limit is due to the [S II] lines on the red side, combined with the Raman wings becoming too weak to measure. The mean H 0 Ly β cross-section corresponding to each band (equation A5) is also given in the table, varying between about 10^{-22} cm^2 and $2 \times 10^{-21} \text{ cm}^2$.

The bands are chosen so as to avoid the strongest contaminating lines wherever possible, but some small contamination is unavoidable, as listed in the rightmost column of the table. The contamination comes from two sources: weak nebular emission lines (indicated by solid vertical lines in Fig. 3) and additionally from the line absorption and emission of the Earth’s atmosphere. Two complementary methods were used to investigate this latter effect. First, the data cube was inspected to identify lines with roughly uniform brightness across the entire map. In particular, any line that is as strong in the Dark Bay region as it is in Orion S is unlikely to come from the nebula itself. Such lines are indicated by vertical dotted lines in Fig. 3 and some are listed in Table 1. Secondly, ESO’s SkyCalc tool² was used to predict theoretical emission and absorption spectra for the atmosphere above the VLT at the time and airmass of the observations, convolved with the MUSE instrumental profile. The emission spectrum is dominated by upper-atmosphere airglow lines of OH (Osterbrock et al. 1996; Noll et al. 2012, 2014), shown in green in the figure, many of which can be seen to coincide with the empirically determined sky lines. The absorption spectrum is dominated by telluric lines of O₂ and H₂O (Moehler et al. 2014; Smette et al. 2015). The strongest predicted absorption near H α is the O₂ γ band at 6280 Å, which is clearly seen in all the spectra, with an absorption depth of order 0.1, but lies well away from the Raman wings. The blue Raman wing is affected by weaker H₂O bands at 6460–6600 Å with absorption depth of <0.01, as compared to the relative brightness of the Raman wings at those wavelengths, which is 0.05–0.1.

In summary, the nebular and telluric contamination introduces uncertainties of order 10 per cent in the fluxes of the B033, B054, and B080 bands, with other bands being affected to a much lesser degree.

2.4 Spatial distribution of Raman band emission

Fig. 4 shows maps of the six innermost Raman bands as two RGB images: the blue wing in panel (a) and the red wing in panel (b). In each case, the channel sequence R, G, B is an inward progression

towards line centre, from the farther wings to the nearer wings. The maps are adaptively smoothed following the binary grid algorithm outlined in García-Díaz et al. (2018), which reduces the noise in the fainter regions at the cost of a reduced spatial resolution. The two maps are strikingly similar, indicating that the contamination of the blue wing (see previous section) is indeed a minor effect when integrated over an entire band.

To aid in the interpretation of the Raman wing maps, Fig. 4(c) shows a combined view of mid-to-low-ionization oxygen emission lines, derived from the MUSE data cube. In blue is shown the [O II] 7318.39, 7319.99 Å doublet, which traces the outer 10 per cent of the fully ionized emission. In green is shown the [O I] 6300.30 Å line, which principally traces partially ionized gas at the ionization front but also shocks in neutral gas.³

In red is shown the fluorescent O I 8446.36 Å line, which traces fully neutral gas that is very close behind the ionization front. This image clearly illustrates that the neutral/molecular gas is organized in linear features, with bright ionization fronts on the side facing the high-mass Trapezium stars. This is most clearly seen in the Orion Bar, the linear emission feature to the south-east of the map, but analogous features are seen in all directions from the Trapezium (see also Fig. 2b). Although the true three-dimensional shape of these bars has not been conclusively established, it is reasonable to assume that they may be cylindrical filaments in three dimensions, possibly related to the ‘fibres’ (Hacar et al. 2018) detected in the molecular gas behind the nebula. A particularly complex region, with several partially overlapping filaments, lies between the Trapezium and the Orion S star formation region. This region shows the brightest Raman wing emission, suggesting that it contains the neutral gas with the highest incident FUV flux, presumably because it lies physically closest to the illuminating high-mass stars.

The spatial relation of the Raman-scattered wings to other emission lines is illustrated in Fig. 4(d), which shows the summed wing intensity over all eight bands as a false colour scale. This is compared with contours that show the ionization front, as traced by the collisionally excited [O I] line, and molecular gas, as traced by the optically thick ¹²CO (1–0) line (Kong et al. 2018). In the Bar region, the Raman emission is clearly seen to be sandwiched between

³The [O I] line is contaminated by airglow emission from the Earth’s upper atmosphere, which I have removed by subtracting the surface brightness measured in portions of the map where the nebula emission is expected to be negligible. Although some residual contamination may remain, a comparison with space-based *HST* observations (O’Dell et al. 1997) shows a good agreement.

²<http://www.eso.org/sci/software/pipelines/skycalc>

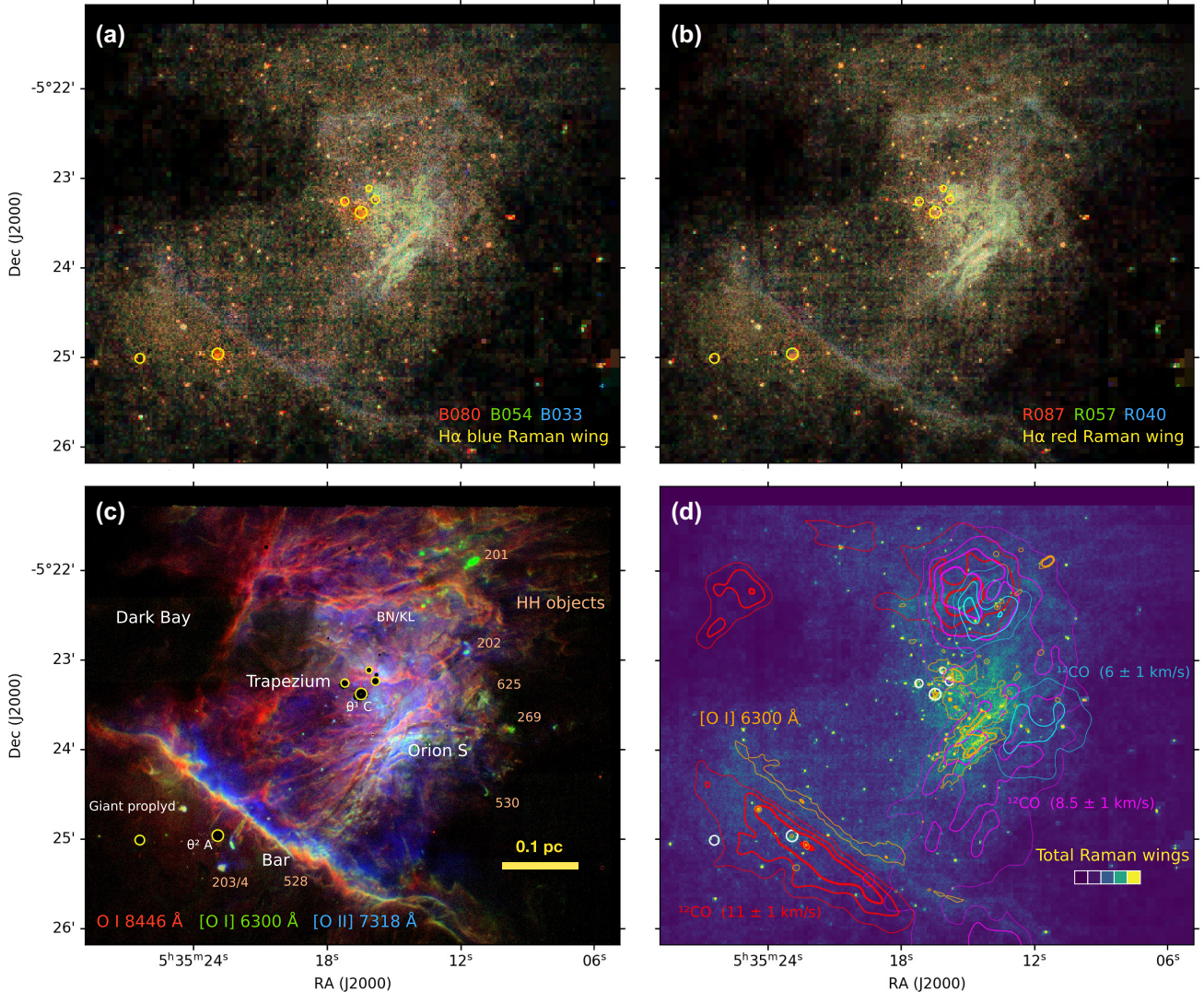


Figure 4. Spatial distribution of Raman-scattered wings of H α . (a) Three-colour RGB image of bands in the blue wing: B080 (red channel), B054 (green), B033 (blue). All bands are continuum-subtracted and are multibinned at constant signal to noise (see text). Maximum brightness in the (red, green, and blue) channels is $(2.27, 3.89, 7.78) \times 10^{-9}$ erg s $^{-1}$ cm $^{-2}$ sr $^{-1}$ Å $^{-1}$. The brightest stars are masked out and marked with yellow circles. Lower mass stars are not masked and most appear as yellow/red dots. (b) Same as (a) but for bands in the red wing: R087 (red), R057 (green), and R040 (blue). (c) Three-colour RGB image of collisional and fluorescent oxygen emission lines that bracket the ionization front: O I $\lambda 8446$ Å (red), [O I] $\lambda 6300$ Å (green), and [O II] $\lambda 7318$ Å (blue). Various features of the nebula are marked, including Herbig–Haro objects driven by jets from young stars. (d) Comparison of the total Raman wing intensity (blue-to-yellow false colour image) with the [O I] emission that traces the ionization front (orange contours) and ^{12}CO emission that traces molecular gas (red, purple, and blue contours for different LSR velocities marked).

the ionization front and the molecular gas, conclusive evidence that it arises in the neutral zone of the PDR. In the Orion S region and around the Trapezium, there is not such a clear stratification between ionized, neutral, and molecular emission. This is due to two factors: first, the densities are higher, which shortens all length scales, and second, the geometry is not so edge-on, leading to a greater degree of superposition along the line of sight, as witnessed by the overlap of the [O I] and ^{12}CO contours. None the less, even here there is evidence that the Raman emission tends to lie farther from θ^1 Ori C than the ionization front, particularly in the ‘SW minibar’ region.

2.5 Emission profiles across the Orion Bar

Fig. 5 shows spatial profiles across the Orion Bar of the Raman-scattered bands (panel a), together with other emission lines and

bands (panels b and c). In keeping with the dominant tradition in the literature (e.g. fig. 9 of van der Werf et al. 1996, fig. 2 of Goicoechea et al. 2017), the molecular regions are shown on the left and the ionized regions on the right. The profiles are the median values across a slit of width 75'', as illustrated in Fig. 5(d). Table 2 shows the positions, widths, and intensities of the peaks in each tracer, as determined by fitting a single Gaussian plus a linear background.

2.5.1 Lines from ionized gas and the ionization front at the Bar

The ionization stratification at the edge of the H II region is clearly seen in the distribution of the [O III], [O II], [O I], and O I lines (Fig. 5c). The peak in [O I] emissivity (excited by collisions between electrons and neutral oxygen atoms) is expected to occur at a hydrogen ionization fraction of 50 per cent (Henney et al. 2005),

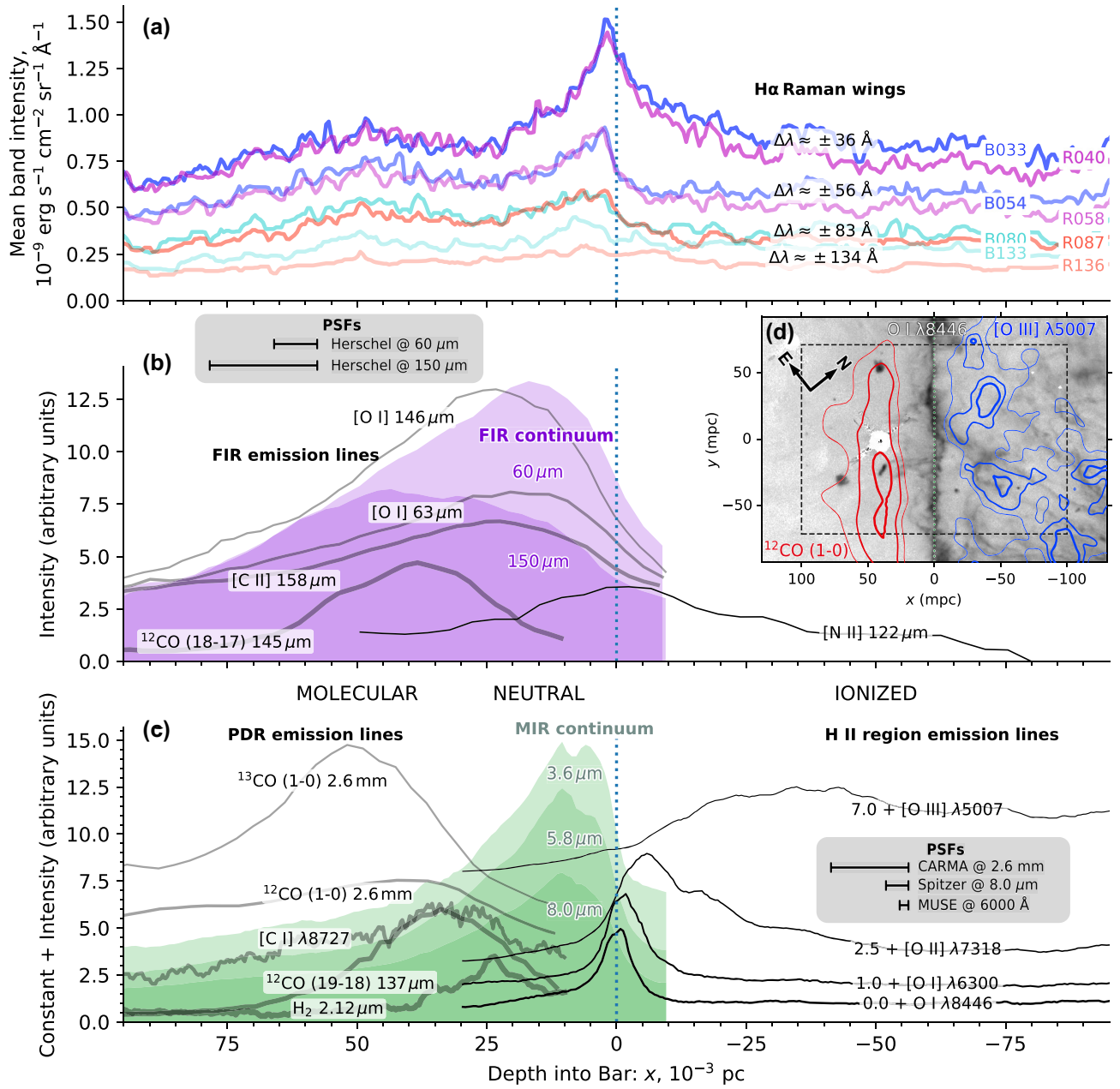


Figure 5. (a) Spatial cut of continuum-subtracted H α wing intensity across the Orion Bar. Matched band pairs from the red and blue wings are shown with the same colour scheme as in Fig. 3. (b) Comparison with far-infrared observations of line and continuum (purple shading) emission from Herschel PACS (Bernard-Salas et al. 2012). The width (FWHM) of the Herschel PSF is shown by horizontal bars for two representative wavelengths. (c) Comparison with a variety of other tracers of molecular, neutral, and ionized material. Optical lines are from VLT MUSE (Weilbacher et al. 2015), infrared continuum bands (green shading) are from Spitzer IRAC (Megeath et al. 2012), CO lines are from Carma-NRO (Kong et al. 2018) and Herschel PACS (Parikka et al. 2018), and H $_2$ near-infrared line is from VLT HAWK-I (Kissler-Patig et al. 2008). (d) Image of the bar in O I , rotated so that the x-axis is along the direction of the spatial cuts (area indicated by dashed rectangle). Contours of molecular CO emission (red) and ionized [O III] emission (blue) are also shown. In all four panels, ultraviolet photons are incident from the right-hand side and the vertical dotted line indicates the ionization front, defined as the peak of the fluorescent O I emission. The profiles are the median values over a slit width of 75'', centred on the ICRS equatorial coordinates $\alpha = 83.8419^\circ$, $\delta = -5.4113^\circ$, and oriented at a position angle of 141.5°. Distances from the ionization front are given in milliparsec (mpc) where 1'' ≈ 1.9 mpc for an assumed distance of (388 ± 5) pc (Kounkel et al. 2017).

which is displaced by $x_0 \approx -1.7$ mpc (milliparsec) from the peak of the O I fluorescent line. This latter should correspond to an absorption optical depth of approximate unity in the FUV pumping lines, such as those listed in Table A1 (see section 5 of Walmsley et al. 2000), corresponding to a neutral hydrogen column density

of $N(\text{H}^0) \approx 10^{19} \text{ cm}^{-2}$ and therefore an average volume density of $n(\text{H}^0) = N(\text{H}^0)/|x_0| \approx 2000 \text{ cm}^{-3}$. This value is similar to the peak electron density on the fully ionized side of the ionization front: $n_e \approx 3000 \text{ cm}^{-3}$, measured from the [S II] 6717/6731 ratio (e.g. O'Dell, Ferland & Peimbert 2017), which occurs at $x \approx -7$ mpc, close to the

Table 2. Peaks in emission profiles across the Orion Bar.

Emission type and units (1)	Line or band (2)	x_0 , mpc (3)	δx , mpc (4)	$I(\text{peak})$ (5)	$I(\text{BG})$ (6)	Ref. (7)
H II region emission lines	[O III] $\lambda 5007$	-32.1 ± 2.6	45	13.059	11.642 ± 5.605	1
	[O II] $\lambda 7318$	-9.4 ± 3.6	25	0.882	0.232 ± 0.026	1
Peak and BG: $\int I_\lambda d\lambda$, $10^{-6} \text{ erg s}^{-1} \text{ cm}^{-2} \text{ sr}^{-1}$	[O I] $\lambda 6300$	-1.7 ± 0.1	9	0.152	0.045 ± 0.001	1
	O I $\lambda 8446$	0.0 ± 0.8	8	0.226	0.071 ± 0.000	2
H α Raman bands	B033	0.8 ± 1.5	20	0.455	0.858 ± 0.007	2
	R040	1.8 ± 0.1	18	0.480	0.815 ± 0.023	
Peak and BG: I_λ , $10^9 \text{ erg s}^{-1} \text{ cm}^{-2} \text{ sr}^{-1} \text{ \AA}^{-1}$	B054	5.0 ± 2.7	9	0.233	0.641 ± 0.009	
	R058	5.5 ± 2.8	11	0.285	0.591 ± 0.017	
	B080	7.1 ± 1.3	11	0.136	0.437 ± 0.013	
	R087	7.1 ± 0.7	15	0.178	0.393 ± 0.017	
	B133	6.7 ± 1.1	10	0.128	0.302 ± 0.004	
	R136	3.1 ± 2.7	27	0.072	0.198 ± 0.007	
Spitzer IRAC bands	$3.6 \mu\text{m}$	11.6 ± 1.1	21	0.200	0.182 ± 0.018	3
Peak and BG: I_ν , GJy sr^{-1}	$5.8 \mu\text{m}$	12.8 ± 2.4	23	1.702	0.966 ± 0.073	
	$8.0 \mu\text{m}$	13.9 ± 3.4	24	4.866	2.622 ± 0.119	
Herschel PACS continuum	$60 \mu\text{m}$	23.9 ± 7.0	52	66.361	25.175 ± 0.261	4
Peak and BG: I_ν , Jy pix^{-1}	$150 \mu\text{m}$	39.2 ± 4.2	63	7.263	2.592 ± 0.065	
PDR emission lines	[N II] $122 \mu\text{m}$	-4.0 ± 1.7	55	1.907	0.581 ± 0.181	4
	[O I] $63 \mu\text{m}$	21.6 ± 1.2	55	1.303	0.823 ± 0.242	
Peak and BG: $\int I_\lambda d\lambda$, median normalized	$\text{H}_2 2.12 \mu\text{m}$	23.6 ± 0.1	19	0.169	0.997 ± 0.002	5
	[C II] $158 \mu\text{m}$	24.3 ± 1.9	47	0.975	0.920 ± 0.145	
	[O I] $146 \mu\text{m}$	26.0 ± 2.8	46	2.299	0.945 ± 0.210	
	$^{12}\text{CO} (19-18)$	33.8 ± 0.1	32	3.930	0.399 ± 0.001	6
	[C I] $\lambda 8727$	37.7 ± 5.9	30	0.495	0.854 ± 0.122	2
	$^{12}\text{CO} (18-17) 145 \mu\text{m}$	38.9 ± 0.5	34	8.193	0.989 ± 0.154	
	$^{12}\text{CO} (1-0)$	41.1 ± 1.2	44	0.472	0.746 ± 0.173	7
	$^{13}\text{CO} (1-0)$	49.8 ± 2.1	33	0.891	0.823 ± 0.112	

Note. Results of fitting a single Gaussian plus linear background to the brightness profiles shown in Fig. 5. COLUMNS: (1) Type of tracer and surface brightness units for the values given in columns 5 and 6. (2) Specific emission line or continuum band. (3) Peak position of fitted Gaussian relative to ionization front. Negative values are on the ionized side of the front, positive values on the neutral/molecular side. The uncertainty is determined as the difference between the fitted Gaussian peak and the actual data peak. (4) FWHM of fitted Gaussian. Note that this is not corrected for the instrumental PSF, which contributes at the 10–20 per cent level in the case of the Herschel and CARMA data (references 4 and 7), but is negligible in other cases. (5) Peak intensity of fitted Gaussian, with brightness units given in column 1. (6) Intensity of fitted background at position $x_0 \pm \delta x$. (7) Data provenance references: 1. VLT–MUSE (Weilbacher et al. 2015); 2. VLT–MUSE (this paper); 3. Spitzer–IRAC (Megeath et al. 2012); 4. Herschel–PACS (Bernard-Salas et al. 2012); 5. VLT–HAWK-I (Kissler-Patig et al. 2008); 6. Herschel–PACS (Parikka et al. 2018); and 7. Carma–NRO (Kong et al. 2018).

peak in the [O II] emission. Therefore, the *total* hydrogen density is roughly constant over the transition between a predominantly ionized state and predominantly neutral state. Note that the apparent width of this transition (for instance, the FWHM of the [O I] peak ≈ 9 mpc) is much larger than predicted by atomic physics, which is probably due to spatial irregularities in the ionization front, which can be seen in the inset in Fig. 5d.

2.5.2 Spatial profiles of the Raman bands in the neutral Bar

Unlike the optical emission lines, the Raman wing bands (upper panel of Fig. 5) all show peaks at positive values of x , corresponding to fully neutral gas in the PDR. There is a very close agreement between corresponding pairs of blue and red bands: B033 with R040, B054 with R058, and B080 with R087. However, there is a systematic tendency for the blue band intensity to be slightly higher than its red counterpart on the ionized side (negative values of x), which is probably due to contamination by nebular emission lines, as listed in column 7 of Table 1. There is a clear tendency for the peak in the brightness profile to progress towards greater depths into the neutral gas as one moves to wavelengths farther from the H α line centre, which is quantitatively confirmed by the Gaussian fits in Table 2.

This result is used as a diagnostic of the PDR density in Section 4.2.3 below.

2.5.3 Other PDR tracers of the neutral and molecular Bar

The left-hand side of panels (b) and (c) of Fig. 5 shows a variety of other emission lines and continuum bands, which trace different layers in the PDR. The near-infrared $\text{H}_2 v = 1 \rightarrow 0 \text{ S}(1)$ line marks the hydrogen dissociation front at $x_0 \approx 24$ mpc (van der Werf et al. 1996; Luhman, Engelbracht & Luhman 1998; Marconi et al. 1998), which provides the outer boundary of the neutral hydrogen layer. Beyond this are found the high- J CO lines, which trace the CO dissociation front at $x_0 \approx 36$ mpc. These coincide with near-infrared [C I] emission, which mainly traces the recombination of C $^+$ ions in cool gas near the dissociation front (Escalante, Sternberg & Dalgarno 1991). The mm-band CO lines trace the deeper, fully molecular regions, with the optically thick $^{12}\text{CO} (1 - 0)$ line at $x_0 \approx 41$ mpc arising outside of the optically thin $^{13}\text{CO} (1 - 0)$ line at $x_0 \approx 50$ mpc (Kong et al. 2018).

The broad infrared bands are dominated by dust emission. For the case of the 3.6–8.0 μm *Spitzer* bands (Megeath et al. 2012), mid-infrared spectroscopy (Bregman et al. 1989; Cesarsky et al.

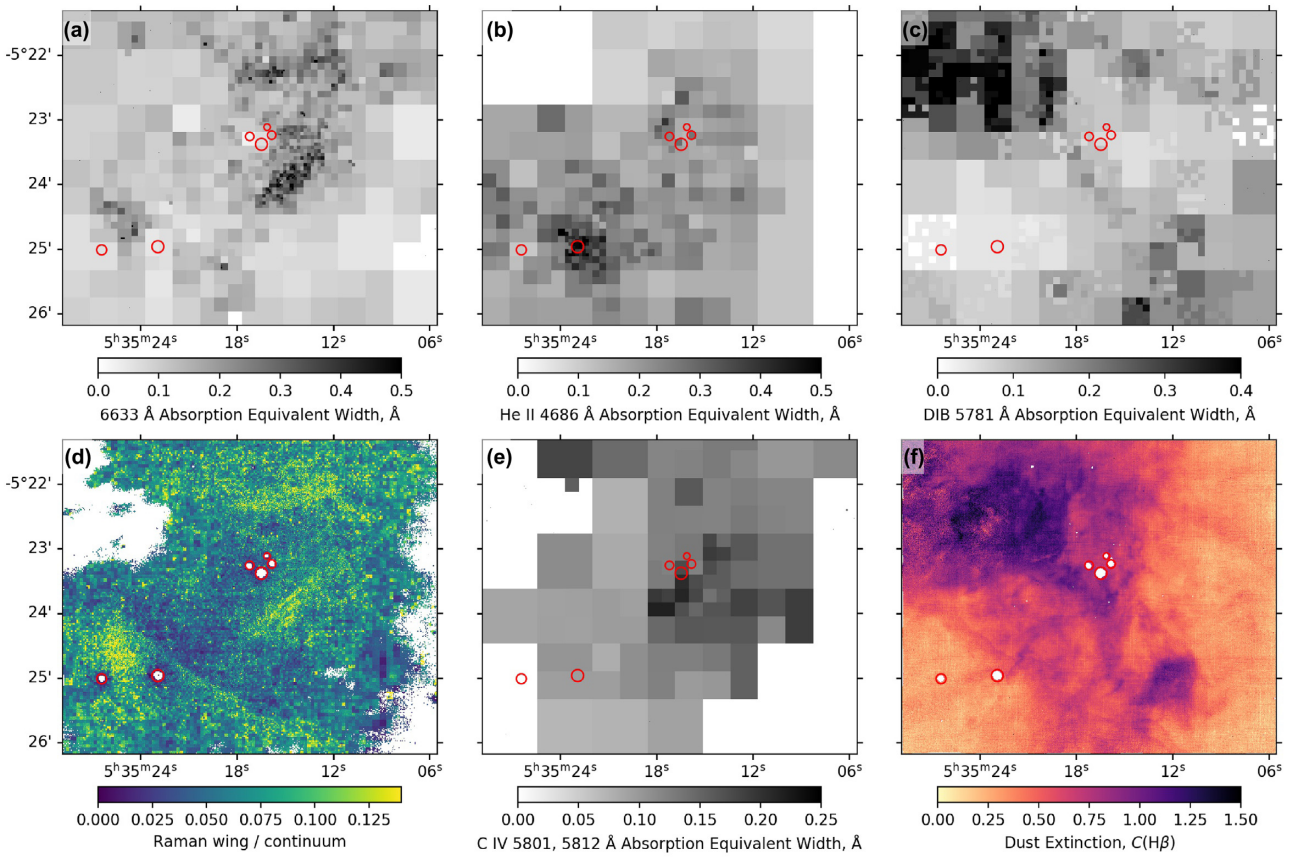


Figure 6. Maps of equivalent widths W_{λ}^{obs} of different absorption features (grey-scale images), compared with maps of other quantities (false colour images). Red circles show positions of bright stars, from West to East: θ^1 Ori A, B, C, D, and θ^2 Ori A, B. (a) Equivalent width of 6633 Å absorption feature. (b) Equivalent width of He II 4685.68 Å absorption line. (c) Equivalent width of a solid-state Diffuse Interstellar Band absorption feature at 5781 Å. (d) Ratio R_{wing} of Raman wing intensity (R058 band) to the intensity of the underlying continuum at the same wavelength. (e) Equivalent width of C IV 5801.35, 5811.97 Å absorption line doublet (sum of the two lines). (f) Foreground dust extinction to the ionized gas, $C(\text{H}\beta)$ (base-10 logarithmic extinction at 4861 Å), calculated from the Balmer decrement $\text{H}\alpha/\text{H}\beta$, assuming the reddening curve of Blagrave et al. (2007).

2000; Kassis et al. 2006) shows that they are mainly due to discrete polycyclic aromatic hydrocarbon (PAH) features at 3.3, 6.2, 7.7, and 8.6 μm , plus a continuum contribution from very small grains (VSGs, with size $a \sim 0.007 \mu\text{m}$, Desert, Boulanger & Puget 1990) and minor contributions from ionized gas lines such as [Ar II] and [Ar III]. The longer wavelength 60 and 150 μm *Herschel* bands (Bernard-Salas et al. 2012) show continuum emission from larger grains ($a \sim 0.1 \mu\text{m}$). The peak of the dust emission moves deeper into the PDR with increasing wavelength, reflecting the decreasing dust temperature as the stellar radiation field is attenuated (Arab et al. 2012).

A complementary view of the Bar is provided by far-infrared emission lines of neutral and ionized metals observed by *Herschel* (Bernard-Salas et al. 2012). The [N II] 122 μm line comes from the H⁺ region and shows a similar distribution to the optical [O II] line. The [C II] 158 μm and [O I] 63 and 146 μm lines, on the other hand, come from the H⁰ region of the PDR.

2.6 Equivalent widths of absorption features

Fig. 6 shows grey-scale maps of the observed equivalent widths, W_{λ}^{obs} , of various absorption features that are found superimposed on the continuous spectrum of the Orion Nebula. These are extracted from the MUSE data cubes by integrating over a short wavelength in-

terval, $\Delta\lambda = \pm 8 \text{ \AA}$, around the central wavelength of the absorption feature:

$$W_{\lambda}^{\text{obs}} = \int_{\Delta\lambda} \frac{I_{\lambda, \text{cont}} - I_{\lambda}}{I_{\lambda, \text{cont}}} d\lambda \quad \text{\AA}, \quad (1)$$

where $I_{\lambda, \text{cont}}$ is the continuum intensity, which is interpolated from the absorption-free portions of the $\Delta\lambda$ interval. Sample spectra that illustrate some of these absorption features are shown in Fig. 7.

2.6.1 Raman-scattered O I 1027 Å

Fig. 6(a) shows W_{λ}^{obs} for the 6633 Å absorption feature, which is a candidate for being a Raman-scattered FUV absorption line. Note that in this case, the ‘continuum’ intensity $I_{\lambda, \text{cont}}$ includes a contribution from the broad Raman wing, as well as the ‘true’ nebular continuum and dust-scattered starlight. Due to the weakness of both the continuum and the absorption line, it was necessary to aggressively bin the data in order to produce an acceptable map. The results in Fig. 6(d) are for a minimum S/N of 7 in W_{λ}^{obs} , which gives the optimum balance between noise and spatial resolution.

The 6633 equivalent width is non-zero across the entire map, with a median value of $W_{\lambda}^{\text{obs}}(6633) \approx 0.1 \text{ \AA}$. It shows peaks of $W_{\lambda}^{\text{obs}}(6633) = 0.3 \pm 0.1 \text{ \AA}$ in exactly the same areas as the peaks in the Raman band emission (see Section 2.4). For ease of comparison,

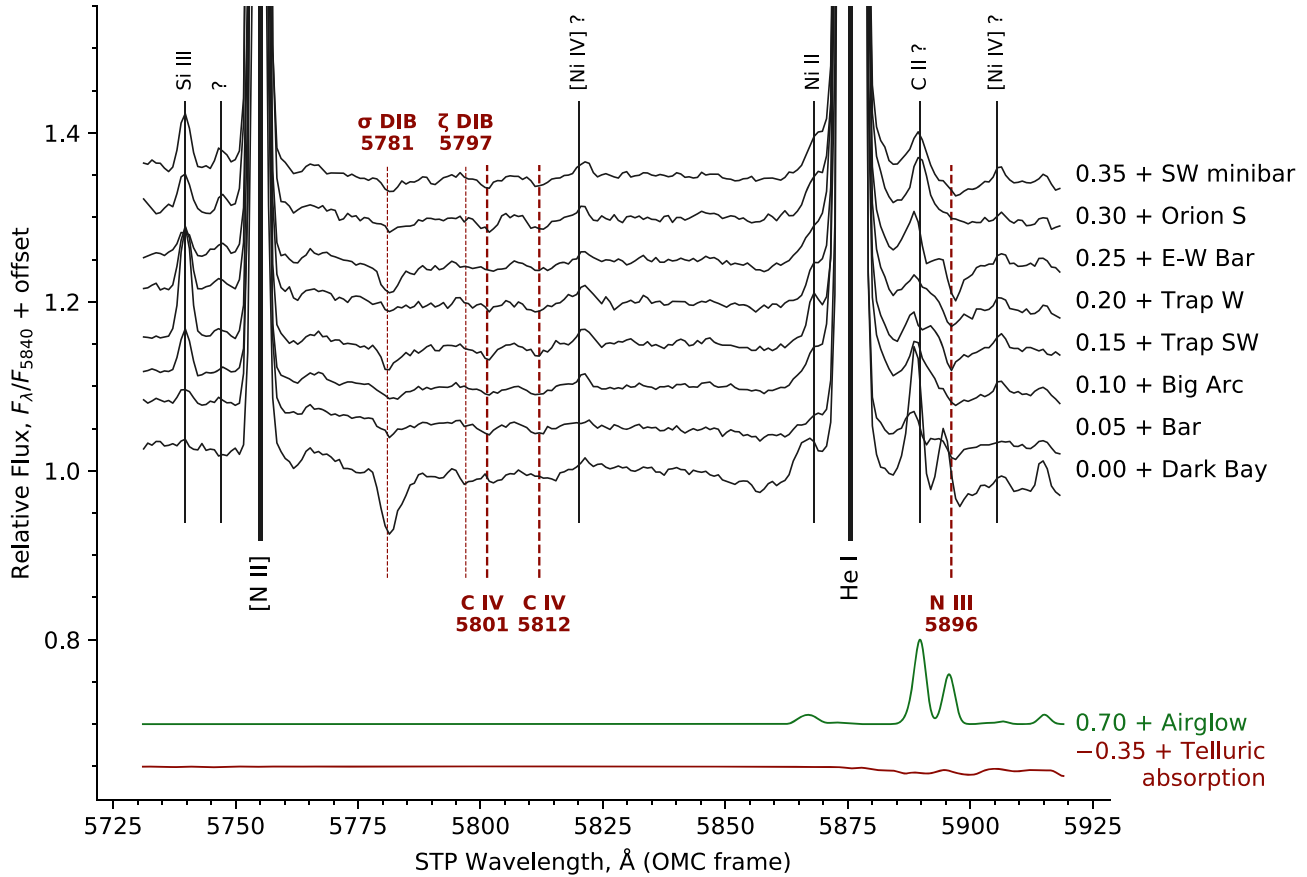


Figure 7. MUSE spectra of the Orion Nebula showing absorption features in the green spectral region, labelled in boldface dark red. Dotted vertical lines indicate the expected wavelengths of Diffuse Interstellar Band features, while dashed vertical lines indicate photospheric lines from OB stars that have been dust-scattered. Selected emission lines are indicated by continuous vertical lines and vertically oriented labels, with tentative or unknown identifications denoted by question marks. All spectra are normalized to the flux at 5840 Å, with offsets for each region as indicated at the right. The spatial regions are the same as shown in Figs 2 and 3. Predicted emission and absorption spectra of the terrestrial atmosphere are shown at the bottom. Note that due to the normalization of the spectra, the apparent brightness of the airglow lines is higher for low surface brightness regions such as the Dark Bay.

Fig. 6(d) shows a map of the wing-to-continuum ratio, R_{wing} , for the R087 red Raman wing band, which is found by dividing the continuum-subtracted intensity in the MUSE data cube by the intensity of the interpolated continuum:

$$R_{\text{wing}} = \frac{\int_{\lambda_{\min}}^{\lambda_{\max}} (I_{\lambda} - I'_{\lambda, \text{cont}}) d\lambda}{\int_{\lambda_{\min}}^{\lambda_{\max}} I'_{\lambda, \text{cont}} d\lambda}, \quad (2)$$

where the band limits λ_{\min} , λ_{\max} are given in Table 1. In this case, the continuum intensity $I'_{\lambda, \text{cont}}$ does not include the Raman wing emission since it is interpolated across a much wider range than in equation (1) by fitting a quadratic function to clean sections of continuum around (6150 ± 80) Å and (6790 ± 30) Å (see Section 2.1). Note also that R_{wing} is a dimensionless ratio, whereas W_{λ}^{obs} has dimensions of wavelength. The reason for choosing the R087 band for this figure is that it is the band that is closest in wavelength to the 6633 Å absorption feature. It is clear from comparing Fig. 6 panels (a) and (d) that $W_{\lambda}^{\text{obs}}(6633)$ and R_{wing} closely track one another, as would be expected if the absorption feature is the Raman-scattered O I 1027 Å line.

The relationship is examined more quantitatively in Fig. 8, which shows that $W_{\lambda}^{\text{obs}}(6633)$ and R_{wing} are well-correlated, with a mean slope of $W_{\lambda} = 2.27 R_{\text{wing}}$. Of the six extraction regions used in Fig. 3, only the Orion Bar lies on this mean relation. The other regions, which are closer to the Trapezium (see Fig. 2b), follow a slope that

is roughly 50 per cent steeper. Although this might represent a real physical difference, it is also true that the lower left area of the graph in Fig. 8 is more susceptible to systematic errors. For instance, in the Orion Bar region much of the continuum comes from the blue reflection nebula around θ^2 Ori A, which causes increased spectral curvature (see Fig. 3), potentially leading to reduced accuracy in the continuum interpolation, which might result in an overestimation of R_{wing} . Higher values of R_{wing} and W_{λ} , such as those seen in Orion S, are much less affected by such uncertainties.

2.6.2 Stellar absorption lines

Fig. 6(b) and (e) show W_{λ}^{obs} for the He II 4685.68 Å absorption line and the C IV 5801.35, 5811.97 Å doublet, respectively. Representative spectra that include the C IV doublet are shown in Fig. 7. Neither of these lines are expected to be seen in emission from the photoionized gas in the nebula due to the high-ionization potentials required. They are therefore well suited for tracing the diffuse dust-scattered starlight in the nebula. It can be seen that the distribution of the two lines is very different. For the He II line, one finds $W_{\lambda}^{\text{obs}}(4686) \approx 0.2$ Å across most of the nebula, but with consistently larger values to the SE, with a pronounced peak of $W_{\lambda}^{\text{obs}}(4686) = (0.4 \pm 0.1)$ Å around the star θ^2 Ori A. In addition,

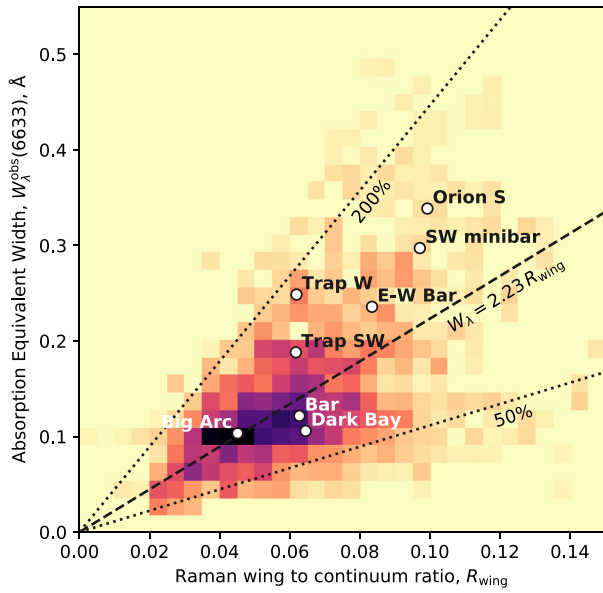


Figure 8. Correlation between 6633 \AA equivalent width, $W_\lambda^{\text{obs}}(6633)$, and Raman wing to continuum ratio, R_{wing} . False-colour image shows histogram of pixels across the face of the nebula, calculated from the MUSE spectral cube: Fig. 6 panel (a) (y-axis) and panel (d) (x-axis). The histogram is weighted by the 6630 \AA continuum intensity. The straight dashed line shows the mean relation, $W_\lambda = 2.27 R_{\text{wing}}$, while dotted lines show a $2 \times$ steeper and $2 \times$ shallower slope. Symbols show average values for each of the extraction regions shown by white boxes in Fig. 2(b).

there is a secondary peak of $W_\lambda^{\text{obs}}(4686) = (0.3 \pm 0.05)\text{ \AA}$, located close to θ^1 Ori D, the easternmost of the four Trapezium stars. In contrast, the C IV lines show a broad maximum of $W_\lambda^{\text{obs}}(5801 + 5812) = (0.16 \pm 0.04)\text{ \AA}$, centred to the SW of the Trapezium.

The most straightforward of these to interpret is C IV, since the 5801,5812 doublet is present in the spectrum of θ^1 Ori C, with a summed equivalent width $W_\lambda^* = (0.44 \pm 0.04)\text{ \AA}$ (Stahl et al. 1996),⁴ but is absent in all the other OB stars in the nebula (as measured from the MUSE data cube). The equivalent width observed in the nebula is smaller than this, because of dilution by the nebular continuum (recombination plus 2-photon) and the starlight from the lower mass members of the Trapezium cluster. The fraction of the total observed continuum intensity that is due to dust scattering of θ^1 Ori C can be estimated as $f_{\text{scat}} = W_\lambda^{\text{obs}}/W_\lambda^*$, for which we find a maximum value of $f_{\text{scat}}(\theta^1\text{ Ori C; C IV}) = 0.4 \pm 0.1$ in the region between the Trapezium and Orion S.

Although θ^1 Ori C (spectral type O7V f?p var; Simón-Díaz et al. 2006; Maíz Apellániz et al. 2019) is the hottest and most luminous star in the nebula, its He II 4686 absorption line is anomalously weak and varies markedly on a rotational time-scale of 15.4 d (Conti 1972; Stahl et al. 1993) because it is partially filled in by emission from the magnetosphere and complex magnetically channelled stellar wind (Donati et al. 2002). From fig. 5 of Stahl et al. (1996), it can be seen that $W_\lambda^*(\theta^1\text{ Ori C; }4686)$ varies systematically from -0.1 \AA to 0.4 \AA as a function of rotational phase.⁵ Three-dimensional simulations (ud-Doula et al. 2013) show that the line profile is dominated by emission ($W_\lambda^* < 0$) for viewing directions along the magnetic pole but by

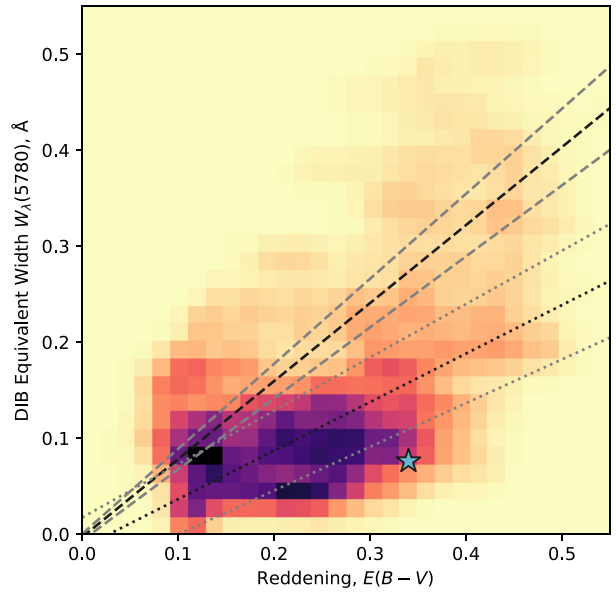


Figure 9. Correlation between DIB equivalent width, $W_\lambda^{\text{obs}}(5780)$, and reddening, $E(B - V)$. False-colour image shows histogram of pixels across the face of the nebula, calculated from the MUSE spectral cube: Fig. 6 panel (c) (y-axis) and panel (f) (x-axis), assuming $E(B - V) = 0.3845 C(H\beta)$. Straight lines show fits to surveys of DIBs along σ -type sightlines to stars (dotted line, Kos & Zwitter 2013) and high-Galactic-latitude sightlines to external galaxies (dashed line, Baron et al. 2015). Star symbol shows result for θ^1 Ori C (Friedman et al. 2011).

photospheric absorption ($W_\lambda^* > 0$) for viewing directions in the magnetic equator. Comparison with observed phase-dependent line profiles suggests that both the line of sight from Earth and the magnetic dipole axis are inclined at $\approx 45^\circ$ from the rotation axis. This implies that the spectrum seen from Earth, integrated over the rotational period, is broadly representative of the average stellar spectrum seen by the surrounding nebula, so that a value of $W_\lambda^*(\theta^1\text{ Ori C; }4686) \approx 0.15\text{ \AA}$ is appropriate, albeit with a large uncertainty.

The second most luminous star in the nebula is the spectroscopic binary θ^2 Ori A (spectral type O9.2V + B0.5:V(n); Maíz Apellániz et al. 2019), located to the SE of the nebula, beyond the Bright Bar. This shows a much simpler He II line profile with $W_\lambda^*(\theta^2\text{ Ori A; }4686) = 0.53\text{ \AA}$ (Simón-Díaz et al. 2006), which explains why $W_\lambda^{\text{obs}}(4686)$ is higher around θ^2 Ori A than around the Trapezium. Applying the same argument as above yields a maximum value of $f_{\text{scat}}(\theta^2\text{ Ori A; He ii}) = 0.75 \pm 0.2$, implying that the blue continuum in this area of the nebula is totally dominated by scattered light from θ^2 Ori A, which forms a roughly circular reflection nebula.

The same absorption line is present in the spectra of other Trapezium stars, being strongest in the B0.5V star θ^1 Ori D with $W_\lambda^*(\theta^1\text{ Ori D; }4686) \approx 0.25\text{ \AA}$ (Simón-Díaz et al. 2006). It is therefore interesting and suggestive that the local peak in $W_\lambda^{\text{obs}}(4686)$ is on θ^1 Ori D's side of the Trapezium. This would not be expected if all the Trapezium stars lay at the same distance from the scattering grains because θ^1 Ori C is four times brighter than θ^1 Ori D at visual wavelengths, so the latter star contributes relatively little to the total luminosity of the Trapezium. However, it has been suggested (O'Dell et al. 1993a; O'Dell 2001; Smith et al. 2005) that θ^1 Ori D may lie closer to the background molecular gas, roughly 0.1 pc behind θ^1 Ori C. In such a case, it would be possible for θ^1 Ori D to dominate the illumination of a small reflection nebula around itself, and the present results would tend to confirm that.

⁴The 10 per cent uncertainty is due to variation with rotational phase, see next paragraph.

⁵Negative equivalent widths correspond to net emission, rather than absorption.

Another stellar absorption line that is visible in the spectra is N III 5896.1 Å, which shows a deeper absorption than the C IV doublet in some parts of the nebula, see Fig. 7. However, its blue flank is badly contaminated by the Na I 5895.923 Å airglow line (see fig. 5 of Osterbrock et al. 1996), so I do not consider it further here.

2.6.3 Diffuse Interstellar Bands

A third type of absorption feature found in the nebular spectrum is what is known as Diffuse Interstellar Bands (DIBs; Heger 1922), of which hundreds are now known (Galazutdinov et al. 2000; Hobbs et al. 2008). The majority are believed to be due to large carbon-based molecules associated with atomic gas (Sonnentrucker 2014) but, apart from in a few instances (Cordiner et al. 2019), their exact nature is still uncertain (Tielens 2014; Omont, Bettinger & T' onshoff 2019; Lai et al. 2020). The strongest such feature found in the MUSE spectra is the well-known band at 5780 Å, which is shown in Fig. 6(c). For comparison, the foreground extinction to the nebula is shown in Fig. 6(f), which is calculated from the H α /H β ratio, assuming the extinction curve of Blagrave et al. (2007).

It is clear at a glance that the spatial distribution of the DIB absorption and the continuum dust extinction are very similar. This is not surprising, since many studies have established a correlation between DIB equivalent widths and interstellar reddening (Friedman et al. 2011; Kos & Zwitter 2013; Baron et al. 2015; Krelowski et al. 2019). It can also be seen in the sample spectra shown in Fig. 7: the deepest DIB absorption is seen for the Dark Bay sample, a high-extinction region in the North East of the nebula. This is tested quantitatively in Fig. 9, which shows the correlation between $W_{\lambda}^{\text{obs}}(5780)$ and dust reddening $E(B - V)$. The relative weakness of the 5797 Å DIB feature in all Orion Nebula sightlines is characteristic of σ -type DIBs (after the prototype σ Sco; Krelowski & Westerlund 1988), which tend to be found in atomic diffuse clouds. I therefore compare the results with a fit to 27 σ -type sightlines to OB stars from the survey of Kos & Zwitter (2013) (dotted line in Fig. 9), which covers the reddening range $E(B - V) = 0.1\text{--}1.2$. I also show (dashed line in figure) a fit to over a million stacked external galaxy and quasar sightlines from SDSS (Baron et al. 2015), which cover the reddening range $E(B - V) = 0\text{--}0.11$. It can be seen that the nebular values follow the general trend of the fits, albeit with considerable dispersion. The tail of high W_{λ} above the fit lines may be due to the fact that a significant fraction of the continuum is dust-scattered and those photons will have traversed a larger column of dust than is measured by the foreground reddening. In addition, the Balmer decrement will saturate at high column densities if part of the dust is mixed with the emitting gas, resulting in an underestimate of $E(B - V)$.

Additional DIB features are seen in the spectral region of the H α Raman wings (see Fig. 3 and Section 2.2). The strongest of these is the 6284 Å feature, but it is difficult to estimate its equivalent width since it overlaps with telluric O₂ γ -band absorption. The 6614 Å feature (Bernstein et al. 2018) is much weaker and is only convincingly detected in the Dark Bay sample. Several other absorption features in the range 6400–6500 Å show correlation with dust extinction and coincide in wavelength with DIB features reported in Galazutdinov et al. (2000).

3 HIGH-RESOLUTION SPECTROSCOPY OF RAMAN-SCATTERED O I 1028 Å

In order to obtain observations of the Raman-scattered O I absorption lines at high spectral resolution, I have searched through archival spectra of the Orion Nebula obtained with the HIRES spectrograph on

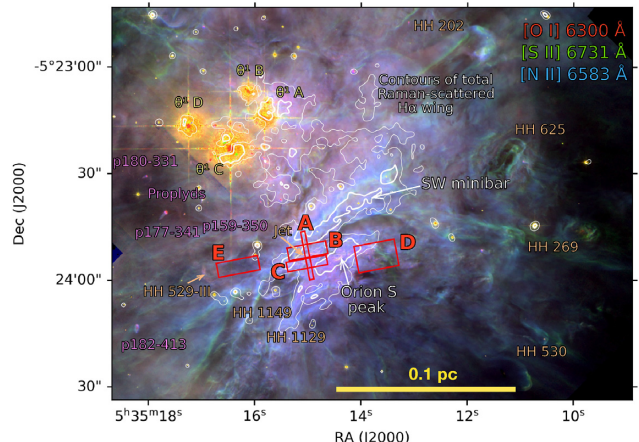


Figure 10. Zoom on Trapezium and Orion South region, showing the locations of extracted Keck spectra (red boxes). The background colour composite image shows *HST* WFPC2 observations in the filters F631N, F673N, and F658N (Bally, O'Dell & McCaughrean 2000), which highlight emission from the ionization front and adjacent regions. White contours show the total Raman-scattered H α wing emission (sum of the six wavelength bands listed in Table 1).

the Keck I telescope (Vogt et al. 1994). The observations, obtained in 1997 December 5 and 6, were targeted at a small number of proplyds and jets in the nebula and are described in detail in Henney & O'Dell (1999) and Bally et al. (2000). Unfortunately, the stronger 6633 Å feature falls in a gap between adjacent spectrograph orders and so was not observed. However, the weaker 6664 Å feature falls in order 53 and is detected in many of the spectra. Results for the proplyds will be presented elsewhere, and I concentrate here on 16 slit positions located in the Orion South region, roughly 30 arcsec SW of the Trapezium. Closely similar slit positions are co-added to improve S/N, forming five groups, A to E, with positions shown in Fig. 10. Most of the slits are 28-arcsec long and 0.574-arcsec wide, but only the central 11 arcsec of order 53 is usable for faint lines due to overlap of adjacent orders.⁶

The broad Raman-scattered wings to H α are spread over several spectrograph orders and uncertainties in the flat-field correction means that it is impossible to separate the wings from the nebular continuum. Therefore, I simply fit a fifth-order polynomial to line-free sections of the spectrum over the entire order (6649–6747 Å) and divide to give a continuum-normalized spectrum. Results for the four groups are shown in Fig. 11 for the wavelength range of interest. A shallow broad absorption feature is clearly seen around 6664 Å in regions A, B, and C, and arguably in region D, while no such feature is seen in region E. At this high spectral resolution (resolving power $R \approx 50\,000$), the absorption line is well separated from the adjacent [Ni II] emission line at 6666.8 Å. From Fig. 10, it can be seen that regions A, B, and C overlap with contours of strong H α wing emission in the SW minibar, while region E lies in a higher ionization part of the nebula, where the H α wing is weak. This is consistent with the observed relative absorption depths, assuming that the 6664 Å feature is due to Raman scattering of the O I 1028.157 29 line (see Table A1).

Table 3 shows results for each slit from fitting both the O I absorption line and the [Ni II] emission line. A single Gaussian component is used for each line and the fits are performed with

⁶One slit in Group A is 14 arcsec long and does not suffer any order overlap.

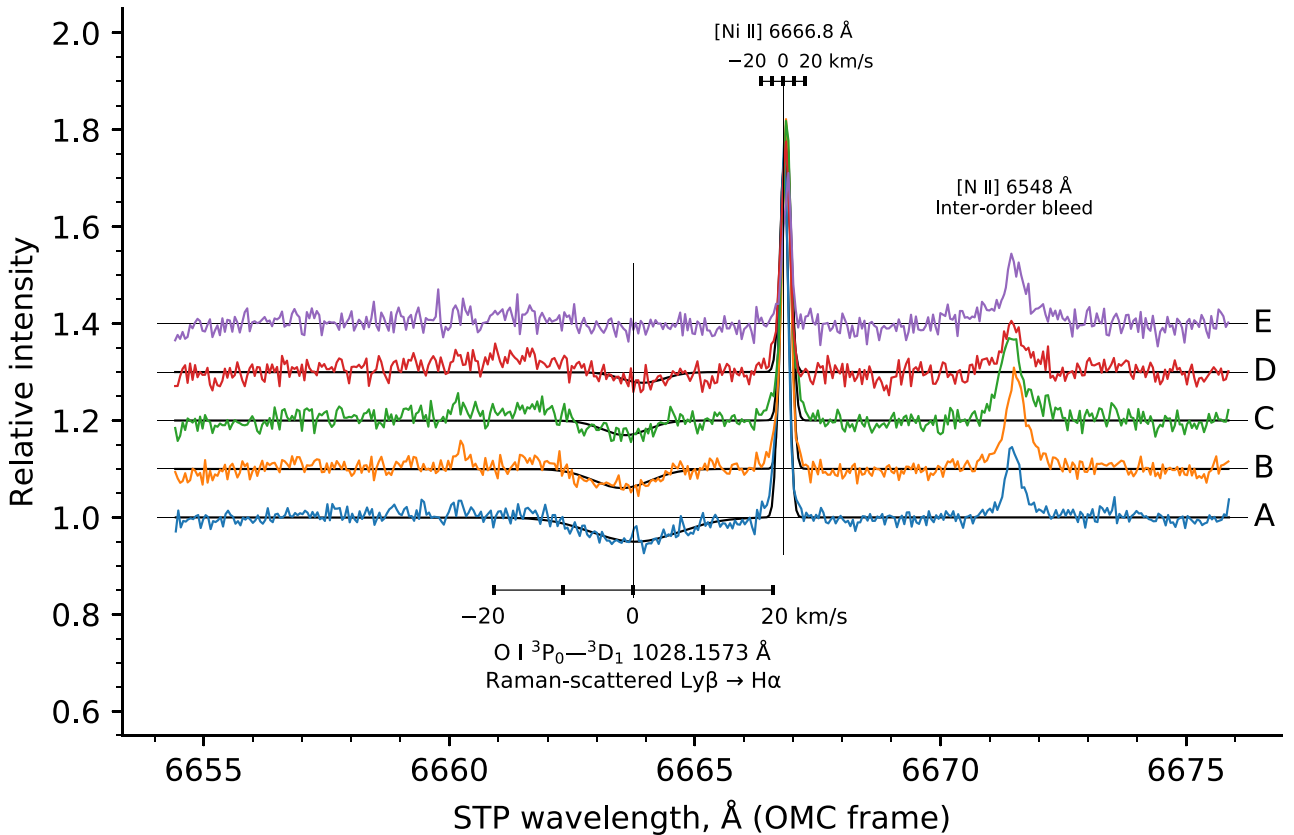


Figure 11. Continuum-normalized Keck HIRES spectra of Raman-scattered O I absorption line for five regions in Orion South. Spectra are offset vertically for ease of comparison. The location of each region is given in Fig. 10. Wavelengths are given on an air scale and in the rest frame of the Orion Molecular Cloud, as defined by the peak velocity of ^{13}CO . Black continuous lines show single-Gaussian fits to the O I absorption line and adjacent [Ni II] emission line, with fit parameters given in Table 3.

the astropy .modeling package.⁷ The O I ultraviolet rest wavelength and its optical counterpart after Raman scattering are discussed in Appendix A, while the [Ni II] rest wavelength comes from hollow cathode tube observations Shenstone (1970). Velocities are given in the reference frame of molecular gas in the Orion South region, as defined by the centroid of ^{13}CO emission (Kong et al. 2018): $V_{\text{LSR}} = (+9.0 \pm 0.2) \text{ km s}^{-1}$ or $V_{\odot} = (+27.1 \pm 0.2) \text{ km s}^{-1}$. Both the emission and absorption lines have velocities that are close to that of the molecular gas, as has been previously found for low-ionization lines in the nebula (e.g. fig. 14 of Baldwin et al. 2000).⁸

The line width is of order 8 km s^{-1} for [Ni II], which is predominantly non-thermal since the thermal broadening is only 3 km s^{-1} for $T = 10^4 \text{ K}$. Compared with other optical emission lines that form near the ionization front, the [Ni II] width is intermediate between the widths of fluorescent lines (e.g. [N I]: $(6 \pm 3) \text{ km s}^{-1}$ Ferland et al. 2012) and collisionally excited lines (e.g. [O I]: $(11.5 \pm 2.6) \text{ km s}^{-1}$ García-Díaz et al. 2008). The Raman-scattered O I line shows the greatest width ($W \approx 15 \text{ km s}^{-1}$) in region A, which is where the absorption is strongest, but is significantly narrower ($W = 7-10 \text{ km s}^{-1}$) in the other regions.

Table 3. Parameters from single-Gaussian line fits to Keck HIRES spectra.

Region (1)	Relative amplitude, A (2)	$V, \text{km s}^{-1}$ (3)	$\Delta V, \text{km s}^{-1}$ (4)
[Ni II] emission 6666.80 Å			
A	0.75 ± 0.02	1.5 ± 0.1	7.7 ± 0.4
B	0.71 ± 0.02	3.7 ± 0.1	7.9 ± 0.4
C	0.60 ± 0.02	4.0 ± 0.2	8.6 ± 0.5
D	0.46 ± 0.01	2.8 ± 0.2	8.5 ± 0.4
E	0.29 ± 0.01	4.6 ± 0.2	6.8 ± 0.6
O I Raman-scattered absorption 6663.75 Å			
A	0.050 ± 0.003	0.4 ± 0.4	14.5 ± 1.0
B	0.039 ± 0.004	-1.4 ± 0.5	9.6 ± 1.1
C	0.030 ± 0.005	-1.0 ± 0.6	7.6 ± 1.5
D	0.022 ± 0.007	1.5 ± 1.0	7.2 ± 2.5

Notes. COLUMNS: (1) Region of nebula covered by HIRES slits (see Fig. 10). (2) Peak emission height or absorption depth relative to continuum. (3) Centroid velocity in frame of molecular cloud. (4) Intrinsic full width at half-maximum line width, after correction for the instrumental width of 6 km s^{-1} . Note that in the case of the O I Raman-scattered absorption line, the centroid velocity and line widths have been divided by 6.4 to account for the stretching of the Doppler scale between the UV and optical frames.

⁷<http://docs.astropy.org/en/stable/modeling/>

⁸Although the [Ni II] line, which likely arises near the ionization front, seems to show a consistent redshift of order 3 km s^{-1} with respect to CO, this is only marginally significant, given that the rest wavelength accuracy of 0.03 \AA corresponds to 1.4 km s^{-1} .

In principle, the kinematics of Raman-scattered lines should be measurable to a higher precision than that of regular lines. This is because the stretching of the Doppler scale means that the effective spectrograph resolving power is multiplied by 6.4 to become

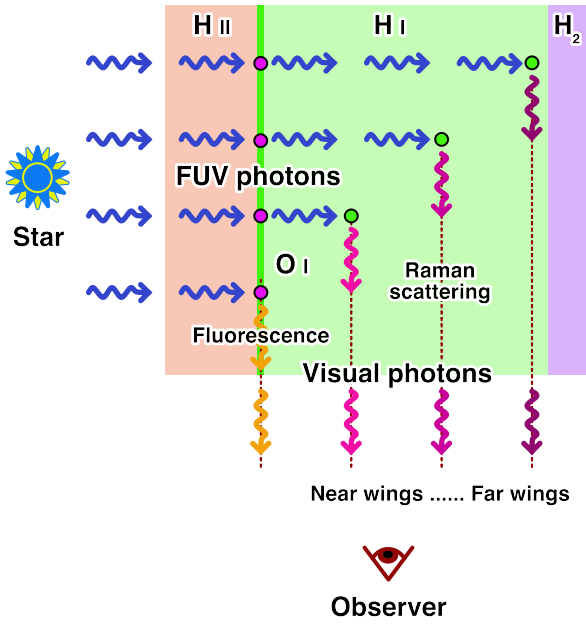


Figure 12. Simplified schematic of where Raman scattering occurs in a PDR. Stellar far-ultraviolet photons (blue wavy arrows) that are far removed in wavelength from resonant H I lines can pass through the photoionized H II layer relatively unscathed. Some of them will be absorbed by metal resonance lines, such as O I (magenta circles) close to the ionization front and fluorescently converted to visual/IR photons (orange wavy arrows). This produces a spectral imprint of the O I absorption on the FUV photons that propagate into the PDR. Once the FUV photons have traversed a sufficient column, they will be non-resonantly scattered by H I (green circles) and a significant fraction will be Raman-converted to visual photons (pink/red wavy arrows). For wavelengths farther from line centre, this Raman scattering occurs deeper in the PDR and is eventually limited by competition from dust absorption and/or the finite total H I column.

$R' = 320\,000$. However, as can be seen from Table 3, the precision of the centroid velocity and width measurements is actually *lower* for O I than for [Ni II].⁹ This is entirely due of the lower signal to noise of the absorption line measurements. Therefore, much longer total exposure times than the 4×300 s of the slits that contribute to region A would be necessary to take full advantage of the boost in spectral resolution provided by Raman scattering.

4 DISCUSSION

In this section, I provide a provisional interpretation of the observational evidence from Sections 2 and 3 in the light of simple heuristic models of Raman scattering, such as is illustrated schematically in Fig. 12. In Section 4.1, I present some formal results from radiative transfer theory that will be used in the following discussion. Section 4.2 investigates how the spatial and spectral characteristics of the broad H α wings can be used to diagnose the physical conditions in the PDR. Section 4.3 considers what extra information can be obtained from the narrow absorption features that are superimposed on the Raman-scattered wings.

⁹The uncertainties are estimated from the parameter covariance array returned by `astropy.modeling.fitting.LevMarLSQFitter`, which uses a least-squares Levenberg–Marquardt algorithm implemented in `scipy.optimize.leastsq` (Virtanen et al. 2020), which in turn is based on the `lmdif` and `lmder` routines in the MINPACK library (Moré 1978).

4.1 Raman radiative transfer

The Raman-scattering process can be divided conceptually into three steps. In step 1, radiative transfer in the FUV band determines the FUV mean intensity, $J_\lambda(\lambda_1)$, at some point in the nebula. In step 2, the scattering itself (see Appendix A) determines a visual-band emission coefficient $j_\lambda(\lambda_2)$ that is proportional to $J_\lambda(\lambda_1)$, where the visual wavelength, λ_2 , and FUV wavelength, λ_1 , are related by equation (A2). In step 3, radiative transfer in the visual band determines the observed intensity of the H α wing, $I_\lambda(\lambda_2)$. I now consider each of these in turn.

If the FUV radiation field at a point is dominated by a single star of luminosity $L_\lambda^*(\lambda_1)$ at a distance R , then for step 1, we may write

$$4\pi J_\lambda(\lambda_1) = \frac{L_\lambda^*(\lambda_1)}{4\pi R^2} e^{-\tau_1} \text{ erg s}^{-1} \text{ cm}^{-2} \text{ \AA}^{-1}, \quad (3)$$

where τ_1 is the FUV optical depth between the point and the star:

$$\tau_1 = \int_0^R k_{\text{total}}(\lambda_1) dR'. \quad (4)$$

The total FUV extinction coefficient can be written as a sum over all absorbing species:

$$k_{\text{total}}(\lambda_1) = \sum_i n_i \sigma_i(\lambda_1) \text{ cm}^{-1}. \quad (5)$$

Potentially important broad-band absorbers are dust grains and the H 0 Rayleigh/Raman scattering itself. Resonance lines of ions, atoms, and molecules may also be important over narrow ranges of λ_1 . More realistically, one would sum over several equations like equation (3) for the different stars and also include the diffuse field due to recombinations, Rayleigh scattering, and dust scattering.

For step 2, assuming that the scattering is isotropic,¹⁰ the visual-band emission coefficient is simply

$$j_\lambda(\lambda_2) = \left(\frac{\lambda_1}{\lambda_2} \right)^3 J_\lambda(\lambda_1) n(H^0) \sigma(\lambda_1) f_{H\alpha}(\lambda_1) \times \text{erg s}^{-1} \text{ cm}^{-3} \text{ sr}^{-1} \text{ \AA}^{-1}, \quad (6)$$

where $n(H^0)$ is the number density of neutral hydrogen atoms, $\sigma(\lambda_1)$ is the Rayleigh-scattering cross-section in the Ly β wing given by equation (A5), and $f_{H\alpha}$ is the branching ratio for Raman conversion given by equation (A6). The factor $(\lambda_1/\lambda_2)^3$ includes one power of λ_1/λ_2 to account for the reduction in energy per photon when passing from the FUV to visual bands, plus two powers of λ_1/λ_2 to account for the transformation of per-angstrom, $d/d\lambda_1 \rightarrow d/d\lambda_2$.

For step 3, the observable intensity, as shown in Figs 4(a, b) and 5(a), is given by an integral over all scattering points z along the line of sight (los):

$$I_\lambda(\lambda_2) = \int_{\text{los}} j_\lambda(\lambda_2) e^{-\tau_2(z)} dz \text{ erg s}^{-1} \text{ cm}^{-2} \text{ sr}^{-1} \text{ \AA}^{-1}, \quad (7)$$

where τ_2 is the visual-band optical depth between each point z and the observer:

$$\tau_2(z) = \int_0^z k_{\text{total}}(\lambda_2) dz'. \quad (8)$$

Similarly to the FUV case, the visual-band extinction coefficient $k_{\text{total}}(\lambda_2)$ can be written as a sum over absorbing species, but the only significant absorber in this case is dust.

¹⁰In reality, the scattering is not quite isotropic but follows the Rayleigh-scattering phase function: $\frac{3}{4}(1 + \cos^2 \theta_{\text{scat}})$, where θ_{scat} is the angle between incident and scattered directions. However, this differs from the isotropic case by 50 per cent or less, so equation (6) is a reasonable approximation.

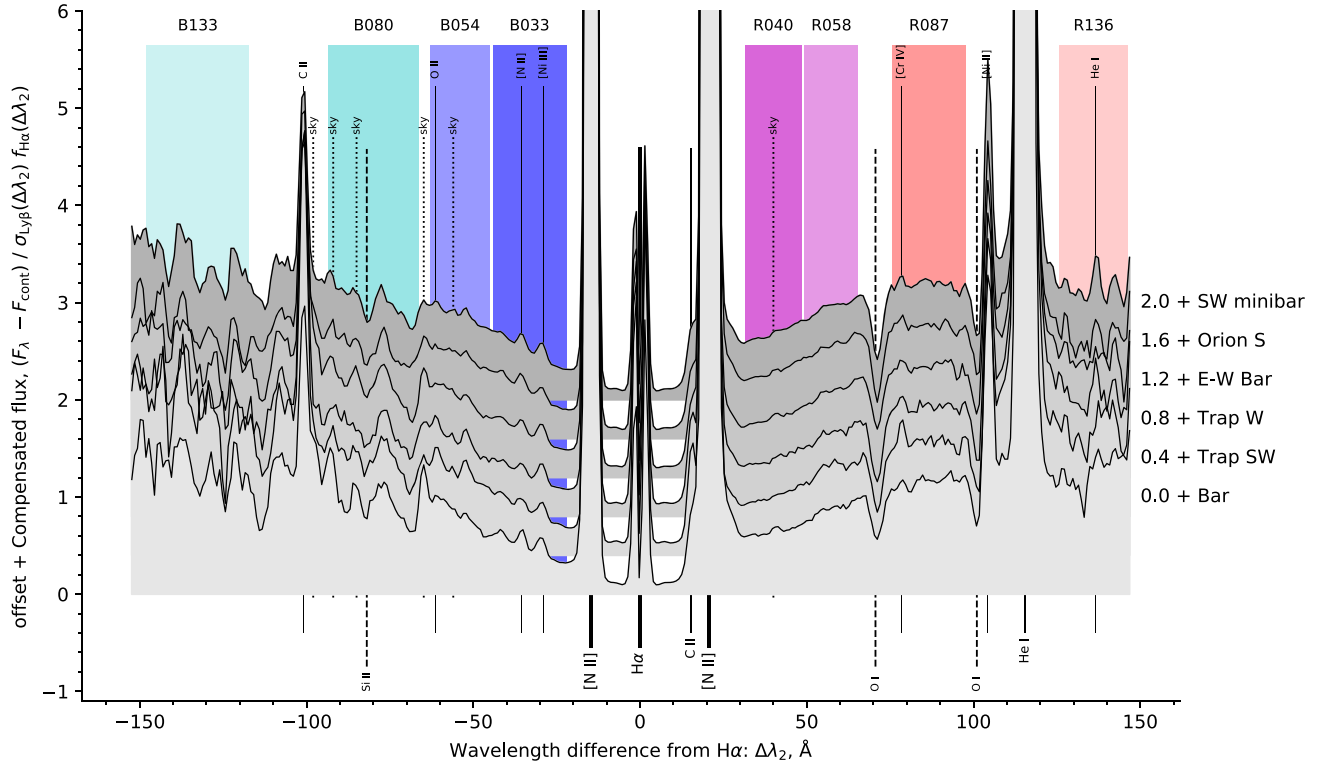


Figure 13. Same as Fig. 3 but with F_λ divided by the effective cross-section to Raman scattering $\sigma f_{H\alpha}$ (see Appendix A) and zoomed in on the Raman wing wavelengths. The spectrum is normalized by the average flux in the R087 band and each region is offset vertically by a constant value, as indicated at right. In this presentation, optically thin Raman scattering of a flat FUV spectrum should give a constant value, which for the Orion data is seen only in the R087 and R136 bands.

4.2 Broad-band Raman scattering

An important question to answer with the Raman scattering is whether it is optically thick or optically thin. There are two optical paths to consider (see previous section): the pre-scattered τ_1 of the FUV photons and the post-scattered τ_2 of the visual-band photons. Of these, it is τ_1 that is most interesting since it is affected not only by dust extinction but also by the opacity of the Rayleigh/Raman scattering itself. The cross-section of the Ly β wings varies by more than an order of magnitude between the different Raman bands (column 6 of Table 1), so it is possible that the nearer wings may be optically thick, while the farther wings are optically thin.

4.2.1 Optically thin limit

For the totally optically thin case, $\tau_1, \tau_2 \ll 1$ (equations 3, 6, and 7) can be combined to yield

$$I_\lambda(\lambda_2) \approx \left(\frac{\lambda_1}{\lambda_2}\right)^3 \sigma(\lambda_1) f_{H\alpha}(\lambda_1) \frac{L_\lambda^*(\lambda_1)}{16\pi^2} \int_{\text{los}} \frac{n(\text{H}^0)}{R^2} dz \times \text{erg s}^{-1} \text{cm}^{-2} \text{sr}^{-1} \text{\AA}^{-1}. \quad (9)$$

When considering the ratio of Raman-scattered intensities between two different wavelengths for the same position on the nebula, the line-of-sight integral cancels and one finds

$$\frac{I_\lambda(\lambda_2)}{\sigma(\lambda_1) f_{H\alpha}(\lambda_1)} \propto L_\lambda^*(\lambda_1). \quad (10)$$

The left-hand side of this equation (approximately $(\Delta\lambda_2)^2 I_\lambda(\lambda_2)$) is plotted in Fig. 13 for the same extraction regions as in Fig. 3.

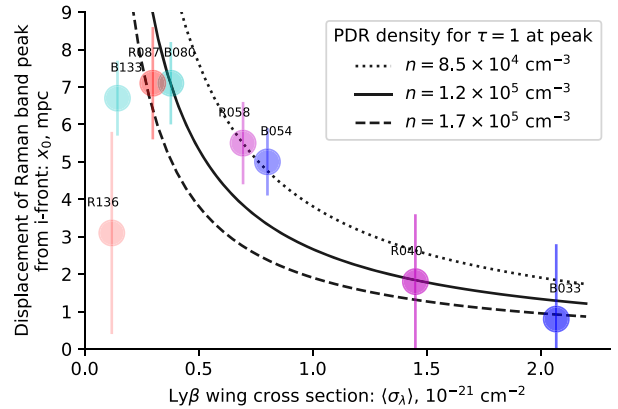


Figure 14. Displacement from the ionization front of the emission peak in each Raman band (column 3 of Table 2), plotted as a function of the cross-section of the Ly β wing (column 6 of Table 1). Colour scheme is as in Fig. 3 with error bars showing 10 per cent of the peak FWHM (column 4 of Table 2). Black lines show a simple model in which the peaks occur at $\tau = 1$ for three different constant neutral hydrogen densities, as indicated in the legend.

For parts of the spectrum where the scattering is optically thin, this should be proportional to the incident FUV spectrum, $L_\lambda^*(\lambda_1)$, which is dominated by the Trapezium OB stars.

It can be seen that the red wing of this compensated spectrum shows an approximately flat section between +80 and +150 Å from H α , covering the R087 and R136 Raman bands. This is consistent with optically thin scattering of a flat FUV spectrum at

these wavelengths. However, the behaviour is not so clear-cut in the blue wing, where the compensated spectrum continues rising away from line centre. Although the slope is slightly shallower in the farther wing (B080 and B133 bands), it never becomes as clearly flat as on the red side. The blue wing is noisier and more contaminated by weak telluric and nebular lines, but this does not seem to be sufficient to explain the discrepancy, which can also be seen in Fig. 3 as a broad ‘shoulder’ in the blue wing, extending from 6300 to 6500 Å. One possibility is that the quadratic function used for continuum interpolation is insufficiently accurate, leading to a systematic overestimate of the strength of the far blue wing. I have investigated the effect of changing the order of polynomial used for the continuum interpolation and find that the intensity of the B080 and B133 bands is quite sensitive to this choice, while the other bands are hardly affected. This might be a result of intermediate scale structure in the dust extinction law (Whiteoak 1966), which has recently been shown to include a broad (≈ 1000 Å) feature centred at 6300 Å (Massa, Fitzpatrick & Gordon 2020).

Closer to the line centre, the results from the two wings are more consistent, with both showing a reduction in compensated intensity. This could mean one of two things: either the Raman wings become optically thick for $|\Delta\lambda_2| < 70$ Å, or the incident FUV spectrum is no longer flat for $|\Delta\lambda_1| < 1.7$ Å, which might correspond to the photospheric Ly β absorption line profile in the spectra of the Trapezium stars.

4.2.2 Optically thick limit

An independent way of discriminating between optically thick and thin scattering is to look at the spatial distribution of the Raman-scattered intensity. In the optically thin limit, this will simply track the spatial distribution of scatterers and so should not vary between the Raman bands. In the optically thick limit, on the other hand, the scattered light will typically arise at $\tau_1 \approx 1$, as I will now demonstrate.

Consider a simplified plane-parallel geometry, as depicted in Fig. 12. The FUV photons (blue wavy lines) propagate horizontally, with τ_1 increasing towards the right. The visual photons propagate vertically (red wavy lines), but I assume here that either τ_2 is small or it is independent of λ_2 , in which case it will have no differential effect between the Raman bands. If the total FUV optical depth is very large, then from equation (3) the mean value of τ_1 weighted by the FUV mean intensity is

$$|\tau_1| = \frac{\int_0^\infty \tau_1 e^{-\tau_1} d\tau_1}{\int_0^\infty e^{-\tau_1} d\tau_1} = 1, \quad (11)$$

where it is also assumed that R does not vary significantly with τ_1 . If, in addition, $n(\mathrm{H}^0)$ and the line-of-sight path-length are roughly constant, then from equations (6 and 7) the mean τ_1 weighted by the observed intensity $I_\lambda(\lambda_2)$ is also $|\tau_1| \approx 1$.

4.2.3 Raman scattering as a diagnostic of the neutral hydrogen density in the PDR

Based on the results of the previous section, one would expect that the peak Raman emission should occur for a Ly β wing optical depth of $\tau_1 \approx 1$ for each band if the scattering is optically thick. Disregarding dust opacity for the time being, this corresponds to a displacement from the ionization front that varies as $x_0 \approx (n(\mathrm{H}^0)\langle\sigma_\lambda\rangle)^{-1}$, where $n(\mathrm{H}^0)$ is the neutral hydrogen density in the PDR and $\langle\sigma_\lambda\rangle$ is the Ly β wing cross-section for the FUV wavelengths that pump each band, which is given in column 6 of Table 1. In Fig. 14, this

relationship is compared with the measurements of the Orion Bar given in Section 2.5, under the assumption that $n(\mathrm{H}^0)$ is constant over the depth range 2–8 mpc. It can be seen that a PDR density of order $n(\mathrm{H}^0) \sim 10^5 \text{ cm}^{-3}$ provides a good fit to the observations for bands within about ± 80 Å of line centre. A systematic uncertainty of 10 per cent of the width of each emission peak is assigned to the x_0 values, which has the largest relative impact on the near-wing bands: B033 and R040. As a result, it is the B054 and R058 bands that are the most reliable indicators, yielding $n(\mathrm{H}^0) = 8.5 \times 10^4 \text{ cm}^{-3}$ (dotted line). This density is similar to that derived from the ratio of intensities of far-infrared [C II] 158-μm and [O I] 145-μm emission lines (Bernard-Salas et al. 2012), which trace slightly deeper layers of the PDR (see Fig. 5 and Table 2). Densities derived from molecular hydrogen emission lines show a great deal of variation: Luhman et al. (1998) find densities of 10^{-5} cm^{-3} to 10^{-6} cm^{-3} , whereas Kaplan et al. (2017) favour densities lower than 10^{-4} cm^{-3} . It has been proposed that the Orion Bar PDR is highly inhomogeneous and clumpy (Burton, Hollenbach & Tielens 1990), but there is little evidence of clumpiness in the distribution of Raman-scattered emission (Fig. 4), nor in the mid-infrared PAH and dust emission (Salgado et al. 2012). This suggests that the shallow regions of the PDR, with column densities up to 10^{-21} cm^{-2} , are relatively smooth.

The displacements of bands in the farther wings fall below the predicted curve, significantly so for B133 and R136. This is an indication that the farther bands may be optically thin instead of optically thick, with the transition occurring near the wavelength of the B080 and R087 bands. It is interesting that this is the same conclusion that is suggested from analysis of the red wing of the compensated spectrum shown in Fig. 13, see Section 4.2.1 above. If this is the case, then it implies that the total H^0 column density through the Orion Bar PDR is $\approx 2 \times 10^{21} \text{ cm}^{-2}$. However, an alternative interpretation could be that in these farther bands, the Ly β wing cross-section falls below the dust absorption cross-section, so that most FUV photons are absorbed by dust before they can be Raman scattered. In this scenario, the implication would be that $\sigma_{\text{dust}} \approx 5 \times 10^{-22} \text{ cm}^2 \text{ H}^{-1}$. It is difficult to discriminate between these two possibilities, especially since the dust opacity probably plays a role in determining the size of the H^0 column via the position of the molecular hydrogen dissociation front (Draine & Bertoldi 1996). The FUV dust absorption cross-section implied by the Raman scattering is slightly lower than predicted for dense clouds (Cardelli, Clayton & Mathis 1989; Weingartner & Draine 2001),¹¹ suggesting that some dust destruction may have occurred in the Orion Bar. Note that Salgado et al. (2016) find that an even lower value of $\sigma_{\text{dust}} \approx 1.6 \times 10^{-22} \text{ cm}^2 \text{ H}^{-1}$ better reproduces the distribution of PAH emission in the Orion Bar. More detailed radiative transfer modelling is required to resolve the issue.

4.3 Absorption features in the Raman pseudo-continuum

The absorption lines seen in the Raman-scattered wings are at STP visual-band wavelengths of $\lambda_2 = 6633$ and 6664 Å, which correspond to vacuum FUV wavelengths of $\lambda_1 = 1027$ and 1028 Å. In Appendix A, it is shown that these can be identified as resonant transitions from the ground state of atomic oxygen: $\mathrm{O} 1 \text{ } 2s2p^4 \ ^3P \rightarrow 2s2p^33d \ ^3D^0$. The implication is that the line absorption occurs before

¹¹For instance, from the modelled extinction cross-sections and albedos of dust with total to selective ratios $R_V = 4.5\text{--}5.5$ (figs 14 and 15 of Weingartner & Draine 2001), the absorption cross-section at Ly β is predicted to be 6.5×10^{-22} to $1.05 \times 10^{-21} \text{ cm}^2$.

the photon is Raman-scattered and therefore contributes to τ_1 (see Section 4.1).

The physical location of this O I absorption is very well constrained observationally because these very same resonance lines (part of the UV 4 multiplet; Moore 1976) are responsible for pumping some of the strongest visual/IR fluorescent emission lines seen in the nebula. Once excited to $3d^3D^0$, the oxygen atom will decay back to the ground level with branching ratio 72.5 per cent via re-emission of an FUV photon, or to the $3p^3P$ level with branching ratio 27.5 per cent via emission of a near-infrared 1.129- μm photon (see fig. 9 of Walmsley et al. 2000).¹² From $3p^3P$, the only option is decay to $3s^3S^0$ via emission of 8446 \AA and then back to ground via emission of 1304 \AA . The spatial distribution of the 8446 \AA emission line (see Figs 4c and 5c) should therefore trace the location of the FUV O I absorption.¹³

It was shown in Section 2 that this fluorescent emission arises very close to the ionization front in all cases and tends to be arranged into filamentary structures that criss-cross the nebula (red channel in Fig. 4c), of which the Orion Bar is the most prominent example. As discussed in Section 2.5.1, the pumping should be most efficient at a hydrogen column density of $\approx 10^{19} \text{ cm}^{-2}$, which is much smaller than the columns of $> 5 \times 10^{20} \text{ cm}^{-2}$ where the Raman scattering occurs.

Note that it has long been recognized (Grandi 1975; Bautista 1999) that it is the stellar continuum radiation that excites the fluorescent O I lines in the Orion Nebula. To the contrary, Dopita et al. (2016) propose that the excitation is due to the Ly β 1025.72 \AA emission line via the coincidence in wavelength with the 1025.76 \AA O I line. However, although this ‘photoexcitation by accidental resonance’ (PAR) process (Kastner & Bhatia 1995) is well attested in novae and Herbig Ae/Be stars (Mathew et al. 2018), it requires the H α transition to be optically thick, which is never the case for H II regions. Powerful empirical arguments against the PAR process operating in the nebula are (1) that 1.316 μm is stronger than 1.129 μm (Walmsley et al. 2000) and (2) the presence of lines originating from O I levels as high as 11s, such as 4980 \AA (Esteban et al. 2004).

4.3.1 Absorption equivalent widths in the FUV frame

The visual-band absorption equivalent width $W_\lambda^{\text{obs}}(6633)$ is tightly correlated with the relative brightness R_{wing} of the Raman wings (Section 2.6.1). Taking the ratio of these, one obtains $W_\lambda^{\text{Raman}}(6633) = W_\lambda^{\text{obs}}(6633)/R_{\text{wing}}$, which is an equivalent width normalized to only the Raman pseudo-continuum itself, rather than the full nebular continuum. This is roughly constant across the nebula at $W_\lambda^{\text{Raman}}(6633) = (2.2 \pm 1.0) \text{ \AA}$ (see Fig. 8). The equivalent width of the FUV absorption line is then smaller than $W_\lambda^{\text{Raman}}(6633)$ by a factor of $(\lambda_2/\lambda_1)^2 \approx 41$, yielding $W_\lambda^{\text{FUV}}(1027) \approx 0.05 \text{ \AA}$. If the line profile is Gaussian, then the relation between velocity FWHM, ΔV , and equivalent width is $W_\lambda = 1.064 A_0 \lambda_0 \Delta V / c$, where A_0 is

¹²In addition, there are some semi-forbidden intercombination transitions that pump the optical forbidden lines, but their branching ratios sum to only 0.003 per cent.

¹³The $3p^3P$ level can also be populated via cascades that originate from pumping of the ns , np , or nd levels with $n \geq 4$. Summing the intensities (in photon units) of all the shorter wavelength O I fluorescent lines that I can find from the observations of Baldwin et al. (2000) and Esteban et al. (2004) and comparing with 8446 \AA implies that 60 per cent of the pumping of $3p^3P$ must come via $3d^3D^0$ or $4s^3S^0$. Given that the 1.129 μm is slightly weaker than 1.316 μm (Walmsley et al. 2000), this means that about 25 per cent of the 8446 \AA emission is caused by absorption of the UV 4 multiplet.

the relative absorption depth at line centre. Assuming complete absorption ($A_0 = 1$) then yields $\Delta V = (15 \pm 6) \text{ km s}^{-1}$. Very similar velocity widths were found for the 6664 \AA absorption feature from the high-resolution Keck spectra (Table 3).

4.3.2 The failure of rival explanations for the 6633, 6664 \AA lines

However strong the case for identifying the absorption features at 6633 and 6664 \AA with Raman-scattered FUV O I absorption lines, it is none the less important to thoroughly investigate potential competing explanations, if only to rule them out.

Why they cannot be dust-scattered stellar absorption lines Various photospheric absorption lines of luminous O stars are visible in the spectrum of the diffuse nebula due to scattering of the starlight by dust grains in the H II region and surrounding PDR. These are clearest in the case of high-ionization lines that are absent from the emission spectrum of the nebular gas, such as the He II and C IV lines that were analysed above in Section 2.6.2. At first glance, it might seem that the equivalent width map of the 6633 \AA feature (Fig. 6a) is similar to that of the C IV absorption lines (Fig. 6e). However, there are important differences: the ridge of peak C IV absorption lies at about 20–30 arcsec from the Trapezium stars, close to the ‘Trap SW’ region shown in Fig. 2(b), whereas the 6633 \AA absorption ridges lie farther from the Trapezium (50–60 arcsec) in the ‘SW minibar’ and ‘Orion S’ regions. This implies that the spatial distribution of scatterers is different between the two cases. This is exactly what would be expected under the Raman-scattering hypothesis for 6633 \AA , since the scatterers are neutral hydrogen atoms, located in the PDR outside the H II region, whereas the stellar continuum is scattered by dust grains, some of which will be inside the H II region.¹⁴

An even stronger argument against a visual-band stellar origin is that no absorption features at 6633 or 6664 \AA are seen in the luminous OB stars of the nebula. The closest match is a pair of Fe I features at 6634 and 6664 \AA , which are seen in absorption in the photospheres of several K and M-type T Tauri stars in the Orion Nebula cluster. One of the brightest and most centrally located examples is V2279 Ori (Parenago 1869, JW 499, TCC 52), a visual binary (spectral type M0.5 + M2; Daemgen, Correia & Petr-Gotzens 2012), which is the central star of the prominent proplyd 159-350 (*HST* 3; O’Dell, Wen & Hu 1993b). However, the luminosity of this source is only $\approx 10 L_\odot$ and its brightness around 6650 \AA is 200 times smaller than that of θ^1 Ori C. Furthermore, photospheric lines are weak in T Tauri stars due to accretion veiling and the equivalent widths of these absorption features are only $W_\lambda^* \approx 0.1 \text{ \AA}$. Therefore, even several such stars would contribute at most 0.001 \AA to the equivalent width in the diffuse nebular spectrum, which is far less than the observed values $W_\lambda^{\text{obs}} = 0.1 \text{ \AA}$ to 0.5 \AA (Fig. 8).

Why they are unlikely to be visual-band neutral/molecular absorption lines from the PDR The fact that the 6633 and 6664 \AA features are not seen in the spectra of the luminous stars, such as θ^1 Ori C, means that they cannot arise in the foreground neutral gas of the Orion veil (Abel et al. 2004; Abel, Ferland & O’Dell 2019).

¹⁴One piece of evidence for the presence of dust inside the H II region is that the gas-phase abundances of nickel and iron are seen to be enhanced in photoionized Herbig–Haro outflows within the nebula (Mesa-Delgado et al. 2009), consistent with dust destruction in shocks. Indirect evidence also comes from the dust-scattered redshifted wing of nebular emission lines (Henney 1998).

However, if some neutral or molecular species were abundant in the dense PDR behind the nebula, but *not* in the Veil, then it is theoretically possible that it might imprint an absorption signature on the starlight that initially enters the PDR but is then reflected out again by dust scattering. On the other hand, such a scenario seems very far-fetched and I have been unable to find any candidate absorption features at relevant wavelengths.

Why they cannot be Diffuse Interstellar Band features The same argument as in the previous paragraph also rules out any possibility that foreground DIB absorption might be responsible for these features, with the additional argument that the 6633 Å equivalent width does not correlate with foreground extinction, as the known DIB at 5780 Å does. However, that leaves open the possibility of the contrived back-scattering scenario discussed above. There is a DIB at 6632.85 Å (Galazutdinov et al. 2000), which is consistent in wavelength with the 6633 Å feature but it is seen only in highly reddened stars and is always at least 10 times weaker than the 5780 Å feature. From Fig. 9, it is conceivable that up to half of the 5780 Å absorption might arise during back-scattering from the PDR rather than in foreground material for some sightlines. This would imply an equivalent width $W_\lambda < 0.02$ Å for the 6632.85 Å DIB, which is again much smaller than the observed $W_\lambda^{\text{obs}}(6633) = 0.1$ to 0.5 Å (Fig. 8).

4.3.3 Possible detection of a 6481 Å absorption feature

A further absorption line is tentatively detected at 6481 Å in the B080 Raman band (see Fig. 3), which could correspond to one of the components of the Si II $3s^23p^2P^o \rightarrow 3s^25s^2S$ doublet (the other component at 6362 Å is hidden by a much stronger [O I] emission line at 6363 Å). This doublet (vacuum FUV wavelengths 1020.7 and 1023.7 Å) pumps the visual-band fluorescent emission lines 5957.6 and 5978.9 Å. The distribution of the 5978.9 Å line is significantly different from the O I fluorescent lines, being more similar to singly ionized forbidden lines such as [S II] and [N II].¹⁵ This is what would be expected since Si⁺, unlike O⁰, has a significant column inside the ionized gas.

The 6481 Å feature is considerably weaker than the other absorption features and is located in a more complicated region of the spectrum, which makes it difficult to make quantitative measurements. Note that Dopita et al. (2016) claim evidence of a broad *emission* bump in the blue Raman wing, centred on the Si II 6481 Å wavelength. However, I find no clear evidence for such a bump in the Orion MUSE or Keck spectra.

5 SUMMARY

By analysing spatially resolved spectroscopic observations of the Orion Nebula, I have demonstrated that the broad Raman-scattered wings of the H α 6563 Å line ($\delta\lambda = \pm 150$ Å) are a useful diagnostic of the interaction of far-ultraviolet radiation with atomic hydrogen in the environs of high-mass stars. The principal conclusions of this study are:

(1) Hydrogen Raman scattering of starlight from Ly β to H α wings occurs in the neutral PDR, located between the hydrogen ionization front and the dissociation front.

(2) The inner Raman wings ($|\delta\lambda| < 80$ Å) of H α are optically thick and allow the density of neutral hydrogen atoms to be determined in

¹⁵The Si II 5957.6 Å line is blended with O I 5958.4 Å and so cannot be used.

edge-on PDRs. For the case of the Orion Bar, I find $n(\text{H}^0) \approx 10^5$ cm⁻³ for the shallow part of the PDR (depths of up to 10 mpc).

(3) The outer Raman wings are either optically thin or are limited by competition with dust absorption. In the first case, the total column density of neutral hydrogen must be 2×10^{21} cm⁻² in the Orion Bar. In the second case, the FUV dust absorption cross-section must be 5×10^{-22} cm² H⁻¹.

(4) Far-ultraviolet resonance lines of neutral oxygen imprint their absorption on to the stellar continuum as it passes through the ionization front. The subsequent Raman scattering of this continuum yields absorption lines in the red H α wing at transformed wavelengths of 6633 Å and 6664 Å. This is a unique signature of Raman scattering, which allows it to be easily distinguished from other processes that might produce broad H α wings, such as electron scattering or high-velocity outflows.

(5) The widths of the Raman-scattered absorption lines are of order 2 Å, which would correspond to a velocity width of 100 km s⁻¹ in the visual band but only 15 km s⁻¹ in the FUV band where the lines were formed. This ‘magnification’ of Doppler velocity scales by the Raman-scattering process allows spectrographs to operate at a 6.4 times higher effective spectral resolution, but observations with better signal to noise than are currently available are required in order to take full advantage of this.

ACKNOWLEDGEMENTS

I am grateful for financial support provided by Dirección General de Asuntos del Personal Académico, Universidad Nacional Autónoma de México, through grant Programa de Apoyo a Proyectos de Investigación e Innovación Tecnológica IN107019. Based on observations collected at the European Southern Observatory under ESO programme 60.A-9100(A). Scientific software and data bases used in this work include SAOImage DS9¹⁶ (Joye & Mandel 2003), the Atomic Line List¹⁷ (Van Hoof 2018), the Cloudy plasma physics code¹⁸ (Ferland et al. 2017), SIMBAD and Vizier from Strasbourg Astronomical Data Center (CDS),¹⁹ and the following 3rd-party Python packages: NUMPY, ASTROPY, MATPLOTLIB, SEABORN, SCIKIT-IMAGE, and REPROJECT. I thank Bob O’Dell for detailed comments on an earlier draft of this paper and I thank the referee Adolf Witt for a prompt, helpful, and illuminating report.

DATA AVAILABILITY

The primary data underlying this article are two spectroscopic data sets. First, integral field spectral mosaics of the inner Orion Nebula, obtained with the MUSE spectrograph on the VLT, which are available from <http://muse-vlt.eu/science/m42/>. Secondly, longslit spectra of the Orion S region, obtained with the HIRES spectrograph on the Keck I telescope, which are available from the Keck Observatory Archive at <https://koa.ipac.caltech.edu/cgi-bin/KOA/nph-KOALogin>. Additional supporting data from other observatories and archives may be accessed via the references given in the main text. All data reduction and analysis programs used in this paper, together with documentation and research notes may be found at <https://github.com/div-B-equals-0/raman-pdr>.

¹⁶<https://sites.google.com/cfa.harvard.edu/saoimageds9>

¹⁷<https://www.pa.uky.edu/~peter/newpage/>

¹⁸<https://nublado.org>

¹⁹<https://cds.u-strasbg.fr>

REFERENCES

- Abel N. P., Brogan C. L., Ferland G. J., O'Dell C. R., Shaw G., Troland T. H., 2004, *ApJ*, 609, 247
- Abel N. P., Ferland G. J., O'Dell C. R., 2019, *ApJ*, 881, 130
- Arab H., Abergel A., Habart E., Bernard-Salas J., Ayasso H., Dassas K., Martin P. G., White G. J., 2012, *A&A*, 541, A19
- Arrieta A., Torres-Peimbert S., 2003, *ApJS*, 147, 97
- Bacon R. et al., 2010, in Proc. SPIE Conf. Ser. Vol. 7735. p. 773508 doi:10.1117/12.856027
- Bacon R. et al., 2014, *Messenger*, 157, 13
- Baldwin J. A., Verner E. M., Verner D. A., Ferland G. J., Martin P. G., Korista K. T., Rubin R. H., 2000, *ApJS*, 129, 229
- Bally J., O'Dell C. R., McCaughrean M. J., 2000, *AJ*, 119, 2919
- Baron D., Poznanski D., Watson D., Yao Y., Prochaska J. X., 2015, *MNRAS*, 447, 545
- Bautista M. A., 1999, *ApJ*, 527, 474
- Bernard-Salas J. et al., 2012, *A&A*, 538, A37
- Bernstein L. S., Shroll R. M., Galazutdinov G. A., Beletsky Y., 2018, *ApJ*, 859, 174
- Blagrave K. P. M., Martin P. G., Rubin R. H., Dufour R. J., Baldwin J. A., Hester J. J., Walter D. K., 2007, *ApJ*, 655, 299
- Bregman J. D., Allamandola L. J., Tielens A. G. G. M., Geballe T. R., Witteborn F. C., 1989, *ApJ*, 344, 791
- Burton M. G., Hollenbach D. J., Tielens A. G. G. M., 1990, *ApJ*, 365, 620
- Cardelli J. A., Clayton G. C., Mathis J. S., 1989, *ApJ*, 345, 245
- Cesarsky D., Jones A. P., Lequeux J., Verstraete L., 2000, *A&A*, 358, 708
- Chang S.-J., Heo J.-E., Di Mille F., Angeloni R., Palma T., Lee H.-W., 2015, *ApJ*, 814, 98
- Clegg R. E. S., Miller S., Storey P. J., Kisielius R., 1999, *A&AS*, 135, 359
- Conti P. S., 1972, *ApJ*, 174, L79
- Cordiner M. A. et al., 2019, *ApJ*, 875, L28
- Da Rio N., Roberto M., Soderblom D. R., Panagia N., Hillenbrand L. A., Palla F., Stassun K., 2009, *ApJS*, 183, 261
- Daemgen S., Correia S., Petr-Gotzens M. G., 2012, *A&A*, 540, A46
- Desert F.-X., Boulanger F., Puget J. L., 1990, *A&A*, 237, 215
- Doi T., O'Dell C. R., Hartigan P., 2004, *AJ*, 127, 3456
- Donati J.-F., Babel J., Harries T. J., Howarth I. D., Petit P., Semel M., 2002, *MNRAS*, 333, 55
- Dopita M. A., Nicholls D. C., Sutherland R. S., Kewley L. J., Groves B. A., 2016, *ApJ*, 824, L13
- Draine B. T., Bertoldi F., 1996, *ApJ*, 468, 269
- Escalante V., Sternberg A., Dalgarno A., 1991, *ApJ*, 375, 630
- Esteban C., Peimbert M., García-Rojas J., Ruiz M. T., Peimbert A., Rodríguez M., 2004, *MNRAS*, 355, 229
- Ferland G. J., Henney W. J., O'Dell C. R., Porter R. L., van Hoof P. A. M., Williams R. J. R., 2012, *ApJ*, 757, 79
- Ferland G. J. et al., 2017, RMxAA, 53, 385
- Friedman S. D. et al., 2011, *ApJ*, 727, 33
- Galazutdinov G. A., Musaev F. A., Krelowski J., Walker G. A. H., 2000, *PASP*, 112, 648
- García-Díaz M. T., Henney W. J., 2007, *AJ*, 133, 952
- García-Díaz M. T., Henney W. J., López J. A., Doi T., 2008, RMxAA, 44, 181
- García-Díaz M. T., Steffen W., Henney W. J., López J. A., García-López F., González-Buitrago D., Áviles A., 2018, *MNRAS*, 479, 3909
- Goicoechea J. R. et al., 2017, *A&A*, 601, L9
- Grandi S. A., 1975, *ApJ*, 199, L43 +
- Greisen E. W., Calabretta M. R., Valdes F. G., Allen S. L., 2006, *A&A*, 446, 747
- Hacar A., Tafalla M., Forbrich J., Alves J., Meingast S., Grossschedl J., Teixeira P. S., 2018, *A&A*, 610, A77
- Heger M. L., 1922, *Lick Obs. Bull.*, 10, 141
- Henney W. J., 1998, *ApJ*, 503, 760
- Henney W. J., O'Dell C. R., 1999, *AJ*, 118, 2350
- Henney W. J., Arthur S. J., Williams R. J. R., Ferland G. J., 2005, *ApJ*, 621, 328
- Hobbs L. M. et al., 2008, *ApJ*, 680, 1256
- Ivanov T. I., Salumbides E. J., Vieitez M. O., Cacciani P. C., de Lange C. A., Ubachs W., 2008, *MNRAS*, 389, L4
- Joye W. A., Mandel E., 2003, in Payne H. E., Jedrzejewski R. I., Hook R. N., eds, ASP Conf. Ser. Vol. 295, Astronomical Data Analysis Software and Systems XII. Astron. Soc. Pac., p. 489
- Kaplan K. F. et al., 2017, *ApJ*, 838, 152
- Kassis M., Adams J. D., Campbell M. F., Deutsch L. K., Hora J. L., Jackson J. M., Tolstrup E. V., 2006, *ApJ*, 637, 823
- Kastner S. O., Bhatia A. K., 1995, *ApJ*, 439, 346
- Kissler-Patig M. et al., 2008, *A&A*, 491, 941
- Kong S. et al., 2018, *ApJS*, 236, 25
- Kos J., Zwitter T., 2013, *ApJ*, 774, 72
- Kounkel M. et al., 2017, *ApJ*, 834, 142
- Krelowski J., Westerlund B. E., 1988, *A&A*, 190, 339
- Krelowski J., Galazutdinov G., Godunova V., Bondar A., 2019, *AcA*, 69, 159
- Lai T. S. Y., Witt A. N., Crawford K., 2017, *MNRAS*, 469, 4933
- Lai T. S. Y., Witt A. N., Alvarez C., Cami J., 2020, *MNRAS*, 492, 5853
- Lee H.-W., Jung Y.-C., Song I.-O., Ahn S.-H., 2006, *ApJ*, 636, 1045
- Luhman K. L., Engelbracht C. W., Luhman M. L., 1998, *ApJ*, 499, 799
- Maíz Apellániz J. et al., 2019, *A&A*, 626, A20
- Marconi A., Testi L., Natta A., Walmsley C. M., 1998, *A&A*, 330, 696
- Marinov D., Booth J. P., Drag C., Blondel C., 2017, *J. Phys. B: At. Mol. Phys.*, 50, 065003
- Martin W. C., Zalubas R., 1983, *J. Phys. Chem. Ref. Data*, 12, 323
- Massa D., Fitzpatrick E. L., Gordon K. D., 2020, *ApJ*, 891, 67
- Mathew B. et al., 2018, *ApJ*, 857, 30
- McLeod A. F., Weilbacher P. M., Ginsburg A., Dale J. E., Ramsay S., Testi L., 2016, *MNRAS*, 455, 4057
- Megeath S. T. et al., 2012, *AJ*, 144, 192
- Mesa-Delgado A., Esteban C., García-Rojas J., Luridiana V., Bautista M., Rodríguez M., López-Martín L., Peimbert M., 2009, *MNRAS*, 395, 855
- Moehler S. et al., 2014, *A&A*, 568, A9
- Mohr P. J., Taylor B. N., Newell D. B., 2008, *Rev. Mod. Phys.*, 80, 633
- Moore C. E., 1976, National Standard Reference Series – National Bureau of Standards., NBS 3, Section 7, Selected Tables of Atomic Spectra, Atomic Energy Levels and Multiplet Tables – O. I. U.S. Department of Commerce, National Bureau of Standards, Washington, DC
- Moré J. J., 1978, in Watson G. A., ed., Numerical Analysis. Springer, Berlin, Heidelberg, p. 105
- Noll S., Kausch W., Barden M., Jones A. M., Szyszka C., Kimeswenger S., Vinther J., 2012, *A&A*, 543, A92
- Noll S., Kausch W., Kimeswenger S., Barden M., Jones A. M., Modigliani A., Szyszka C., Taylor J., 2014, *A&A*, 567, A25
- Nussbaumer H., Schmid H. M., Vogel M., 1989, *A&A*, 211, L27
- O'Dell C. R., 2001, *ARA&A*, 39, 99
- O'Dell C. R., Yusef-Zadeh F., 2000, *AJ*, 120, 382
- O'Dell C. R., Valk J. H., Wen Z., Meyer D. M., 1993a, *ApJ*, 403, 678
- O'Dell C. R., Wen Z., Hu X., 1993b, *ApJ*, 410, 696
- O'Dell C. R., Hartigan P., Lane W. M., Wong S. K., Burton M. G., Raymond J., Axon D. J., 1997, *AJ*, 114, 730
- O'Dell C. R., Ferland G. J., Peimbert M., 2017, *MNRAS*, 464, 4835
- Omont A., Bettinger H. F., T'Onshoff C., 2019, *A&A*, 625, A41
- Osterbrock D. E., Ferland G. J., 2006, Astrophysics of Gaseous Nebulae and Active Galactic Nuclei, 2nd edn. University Science Books, Sausalito, CA
- Osterbrock D. E., Fulbright J. P., Martel A. R., Keane M. J., Trager S. C., Basri G., 1996, *PASP*, 108, 277
- Parikka A., Habart E., Bernard-Salas J., K'ohler M., Abergel A., 2018, *A&A*, 617, A77
- Pequignot D., Baluteau J. P., Morisset C., Boisson C., 1997, *A&A*, 323, 217
- Perrin J. M., Sivan J. P., 1992, *A&A*, 255, 271
- Salgado F. et al., 2012, *ApJ*, 749, L21
- Salgado F., Berné O., Adams J. D., Herter T. L., Keller L. D., Tielens A. G. G. M., 2016, *ApJ*, 830, 118
- Schmid H. M., 1989, *A&A*, 211, L31
- Schmidt G. D., Cohen M., Margon B., 1980, *ApJ*, 239, L133
- Shenstone A. G., 1970, *J. Res. Natl. Bur. Stand. Sect. A Phys. Chem.*, 74A, 801

- Simón-Díaz S., Herrero A., Esteban C., Najarro F., 2006, *A&A*, 448, 351
 Smette A. et al., 2015, *A&A*, 576, A77
 Smith N., Bally J., Shuping R. Y., Morris M., Kassis M., 2005, *AJ*, 130, 1763
 Sonnentrucker P., 2014, in Cami J., Cox N. L. J., eds, Proc. IAU Symp. 297, The Diffuse Interstellar Bands. p. 13 doi:10.1017/S1743921313015524
 Stahl O., Wolf B., Gang T., Gummelsbach C. A., Kaufer A., Kovacs J., Mandel H., Szeifert T., 1993, *A&A*, 274, L29
 Stahl O. et al., 1996, *A&A*, 312, 539
 Subrahmanyam R., Goss W. M., Malin D. F., 2001, *AJ*, 121, 399
 Tiensl A. G. G. M., 2014, in Cami J., Cox N. L. J., eds, Proc. IAU Symp. 297, The Diffuse Interstellar Bands. p. 399 doi:10.1017/S1743921313016207
 ud-Doula A., Sundqvist J. O., Owocki S. P., Petit V., Townsend R. H. D., 2013, *MNRAS*, 428, 2723
 van der Werf P. P., Stutzki J., Sternberg A., Krabbe A., 1996, *A&A*, 313, 633
 Van Hoof P. A. M., 2018, *Galaxies*, 6
 Virtanen P. et al., 2020, *Nature Methods*, 17, 261
 Vogt S. S. et al., 1994, in Crawford D. L., Craine E. R., eds, Proc. SPIE Conf. Ser. Vol. 2198, Instrumentation in Astronomy VIII. SPIE, p. 362 doi:10.1117/12.176725
 Walmsley C. M., Natta A., Oliva E., Testi L., 2000, *A&A*, 364, 301
 Weilbacher P. M. et al., 2015, *A&A*, 582, A114
 Weingartner J. C., Draine B. T., 2001, *ApJ*, 548, 296
 Whiteoak J. B., 1966, *ApJ*, 144, 305
 Witt A. N., Lai T. S. Y., 2020, *Ap&SS*, 365, 58

APPENDIX A: RAMAN-SCATTERING THEORY

When a photon is Raman-scattered from the vicinity of Ly β (UV domain) to the vicinity of H α (optical domain), its wavelength is transformed from λ_1 to λ_2 . Intervals in frequency ($v = c/\lambda$) or wavenumber ($\tilde{v} = 1/\lambda$) space are conserved between the two domains. For example, the wavenumber displacement from the H i line centre can be written in two ways:

$$\Delta\tilde{v} = \tilde{v}_1 - \tilde{v}(\mathrm{Ly}\beta) = \tilde{v}_2 - \tilde{v}(\mathrm{H}\alpha), \quad (\text{A1})$$

from which it follows that

$$\lambda_2 = \left(\frac{1}{\lambda(\mathrm{H}\alpha)} + \frac{1}{\lambda_1} - \frac{1}{\lambda(\mathrm{Ly}\beta)} \right)^{-1}. \quad (\text{A2})$$

The wavelengths $\lambda(\mathrm{Ly}\beta)$ and $\lambda(\mathrm{H}\alpha)$, together with their corresponding wavenumbers, are given in Table A1 (all wavelengths are on the vacuum scale unless otherwise noted). For both lines, a weighted average over the $3p^2P_{1/2}$ and $3p^2P_{3/2}$ upper levels is used, assumed to be populated according to their statistical weights, with individual component wavelengths obtained from table XXVIII of Mohr, Taylor & Newell (2008). Note that the electric dipole selection rules mean that only $3p \rightarrow 2s$ transitions contribute to H α in the Raman-scattering context. The wavelength is therefore slightly shorter than the value obtained for the H α recombination line, which includes additional contributions from $3s \rightarrow 2p$ and $3d \rightarrow 2p$. The shift is of order -0.05 \AA or -2 km s^{-1} with respect to the Case B results reported in table 6a of Clegg et al. (1999).

Also listed in Table A1 are the Raman transformations $\lambda_1 \rightarrow \lambda_2$ for the rest wavelengths of transitions between the ground $2s^22p^43P$ term of neutral $^{16}\mathrm{O}$ and the excited $2s^22p^33d^3D^0$ term. The O i data are obtained from highly accurate laser metrology (Ivanov et al. 2008; Marinov et al. 2017), with a precision of 0.08 cm^{-1} or better. The fine structure splitting between the J_k levels of the excited term ($\sim 0.1 \text{ cm}^{-1}$) is much smaller than that between the J_i levels of the ground term ($\sim 100 \text{ cm}^{-2}$), so that the six transitions fall into three well-separated groups. The three transitions from the lowest energy $J_i = 2$ level are very close to Ly β ($\Delta\tilde{v} \approx 4 \text{ cm}^{-1}$), whereas the two transitions from $J_i = 1$ ($\Delta\tilde{v} \approx 162 \text{ cm}^{-1}$) and the single transition from $J_i = 0$ ($\Delta\tilde{v} \approx 231 \text{ cm}^{-1}$) lie increasingly to

the red. The corresponding wavelengths in the optical domain, λ_2 , are therefore on the red side of H α . The final column of the table uses STP refractive indices (Greisen et al. 2006) to convert λ_2 to air wavelengths, λ_{air} , for ease of comparison with ground-based optical spectroscopy. The resultant wavelength is 6663.747 \AA for the line from $J_i = 0$, with an uncertainty of about 0.004 \AA , which is much smaller than typical observational precision (for instance, 0.07 \AA for a very high-resolution spectrograph with resolving power of $R = 10^5$). The two lines from $J_i = 1$, with a separation of 0.028 \AA , will always be blended in observations, giving a mean wavelength of 6633.347 \AA (assuming the upper levels are distributed according to statistical weight $2J_k + 1$). Similarly, the three lines from $J_i = 2$ have a mean wavelength of 6564.386 \AA , but this is so close to H α (corresponding to a Doppler shift of $+75 \text{ km s}^{-1}$) that it would be very difficult to observe.

The final section of Table A1 gives data for a resonance doublet of Si $^+$ whose components lie a few \AA to the blue of Ly β . The shorter of the two components is Raman-transformed to $\lambda_{\mathrm{air}} = 6362.35 \text{ \AA}$, which unfortunately coincides with the collisionally excited [O I] line at 6363.78 \AA . The longer component is transformed to 6480.81 \AA in a region that is clear of any strong nebular lines. Wavelengths for these lines are based on energy levels from Martin & Zalubas (1983), with an estimated precision of 0.1 cm^{-1} , which gives an uncertainty in the optical wavelengths λ_2 of 0.04 \AA .

The total cross-section for the off-resonance $1s \rightarrow 3p$ transition in H 0 is calculated in section 2 of Chang et al. (2015) from second-order time-dependent perturbation theory. Results are presented in the upper panel of fig. 1 of that paper in terms of a Doppler velocity factor ΔV_1 , which in the notation of the current paper is

$$\Delta V_1 = c \left(\frac{\lambda_1}{\lambda(\mathrm{Ly}\beta)} - 1 \right). \quad (\text{A3})$$

The observed Raman-scattered wings of H α that are analyzed in this paper are typically within $\Delta\lambda_2 \sim \pm 100 \text{ \AA}$ of the line core. It is therefore convenient to define a dimensionless wavelength in the optical domain as

$$x = \frac{\lambda_2 - \lambda(\mathrm{H}\alpha)}{100 \text{ \AA}}, \quad (\text{A4})$$

which corresponds to $x \approx \Delta V_1 / 714 \text{ km s}^{-1}$ in the FUV domain. The total cross-section in the range $0.4 < |x| < 2.3$ can then be fit as follows:

$$\frac{\sigma}{10^{21} \text{ cm}^2} = \begin{cases} 0.2186x^{-2} - 0.0344x^{-1} - 0.0054 & \text{if } x < 0 \\ 0.2367x^{-2} - 0.0187x^{-1} + 0.0004 & \text{if } x > 0 \end{cases}. \quad (\text{A5})$$

Note that separate fits are given for the blue ($x < 0$) and red ($x > 0$) wings of H α since the cross-section, although approximately Lorentzian, is not exactly symmetric, being stronger on the blue side (by about 10 per cent for $x = \pm 1$).

The fraction of all $1s \rightarrow 3p$ excitations that result in Raman scattering to an optical photon is given by the branching ratio, $f_{\mathrm{H}\alpha}$, with the remaining fraction, $1 - f_{\mathrm{H}\alpha}$, resulting in elastic Rayleigh scattering in which the photon remains in the FUV domain. The results for $f_{\mathrm{H}\alpha}$ are also shown in fig. 1 of Chang et al. (2015) and can be fit as follows in the range $|x| < 5$:

$$f_{\mathrm{H}\alpha} = 0.2238 + 0.0363x + 0.0024x^2. \quad (\text{A6})$$

The relative accuracy of all these fits is better than 1 per cent within the stated range (corresponding to $\sigma \approx 10^{-22} \text{ cm}^2$ to 10^{-21} cm^2), which is perfectly adequate for the purposes of this paper. Note that the branching ratio increases with x , which means that the product $\sigma f_{\mathrm{H}\alpha}$ is stronger on the red side of H α .

Table A1. FUV/optical wavelength equivalencies for Raman scattering.

Ion	transition	$J_i \rightarrow J_k$	$\lambda_1, \text{\AA}$	$\tilde{v}_1, \text{cm}^{-1}$	$\Delta\tilde{v}, \text{cm}^{-1}$	$\tilde{v}_2, \text{cm}^{-1}$	$\lambda_2, \text{\AA}$	$\lambda_{\text{air}}, \text{\AA}$
		 Ly $\beta, n = 1$	H $\alpha, n = 2$
H I	ns ² S → 3p ² P	1/2 → 1/2, 3/2	1025.72220	97492.283	0.000	15233.329	6564.553	6562.740
O I	2s ² 2p ⁴ 3P → 2s ² 2p ³ (⁴ S)3d ³ D ⁰	0 → 1	1028.15729	97261.383	-230.900	15002.429	6665.587	6663.747
		1 → 1	1027.43139	97330.100	-162.183	15071.146	6635.196	6633.364
		1 → 2	1027.43077	97330.159	-162.124	15071.205	6635.170	6633.338
		2 → 1	1025.76339	97488.369	-3.914	15229.415	6566.240	6564.427
		2 → 2	1025.76276	97488.429	-3.854	15229.475	6566.215	6564.401
		2 → 3	1025.76170	97488.530	-3.753	15229.576	6566.171	6564.358
Si II	3s ² 3p ² P ⁰ → 3s ² 5s ² S	1/2 → 1/2	1020.6989	97972.086	+479.803	15713.132	6364.104	6362.345
		1/2 → 3/2	1023.7001	97684.859	192.576	15425.905	6482.602	6480.811

This paper has been typeset from a $\text{T}_{\text{E}}\text{X}/\text{L}\text{A}_{\text{T}}\text{E}\text{X}$ file prepared by the author.

List of astronomical key words (Updated on 2020 January)

This list is common to *Monthly Notices of the Royal Astronomical Society*, *Astronomy and Astrophysics*, and *The Astrophysical Journal*. In order to ease the search, the key words are subdivided into broad categories. No more than six subcategories altogether should be listed for a paper.

The subcategories in boldface containing the word ‘individual’ are intended for use with specific astronomical objects; these should never be used alone, but always in combination with the most common names for the astronomical objects in question. Note that each object counts as one subcategory within the allowed limit of six.

The parts of the key words in italics are for reference only and should be omitted when the keywords are entered on the manuscript.

General

editorials, notices
errata, addenda
extraterrestrial intelligence
history and philosophy of astronomy
miscellaneous
obituaries, biographies
publications, bibliography
sociology of astronomy
standards

radiation: dynamics
radiation mechanisms: general
radiation mechanisms: non-thermal
radiation mechanisms: thermal
radiative transfer
relativistic processes
scattering
shock waves
solid state: refractory
solid state: volatile
turbulence
waves

Physical data and processes

acceleration of particles
accretion, accretion discs
asteroseismology
astrobiology
astrochemistry
astroparticle physics
atomic data
atomic processes
black hole physics
chaos
conduction
convection
dense matter
diffusion
dynamo
elementary particles
equation of state
gravitation
gravitational lensing: micro
gravitational lensing: strong
gravitational lensing: weak
gravitational waves
hydrodynamics
instabilities
line: formation
line: identification
line: profiles
magnetic fields
magnetic reconnection
(magnetohydrodynamics) MHD
masers
molecular data
molecular processes
neutrinos
nuclear reactions, nucleosynthesis, abundances
opacity
plasmas
polarization

Astronomical instrumentation, methods and techniques
atmospheric effects
balloons
instrumentation: adaptive optics
instrumentation: detectors
instrumentation: high angular resolution
instrumentation: interferometers
instrumentation: miscellaneous
instrumentation: photometers
instrumentation: polarimeters
instrumentation: spectrographs
light pollution
methods: analytical
methods: data analysis
methods: laboratory: atomic
methods: laboratory: molecular
methods: laboratory: solid state
methods: miscellaneous
methods: numerical
methods: observational
methods: statistical
site testing
space vehicles
space vehicles: instruments
techniques: high angular resolution
techniques: image processing
techniques: imaging spectroscopy
techniques: interferometric
techniques: miscellaneous
techniques: photometric
techniques: polarimetric
techniques: radar astronomy
techniques: radial velocities
techniques: spectroscopic
telescopes

Astronomical data bases

astronomical data bases: miscellaneous
atlases
catalogues
surveys
virtual observatory tools

Software

software: data analysis
software: development
software: documentation
software: public release
software: simulations

Astrometry and celestial mechanics

astrometry
celestial mechanics
eclipses
ephemerides
occultations
parallaxes
proper motions
reference systems
time

The Sun

Sun: abundances
Sun: activity
Sun: atmosphere
Sun: chromosphere
Sun: corona
Sun: coronal mass ejections (CMEs)
Sun: evolution
Sun: faculae, plages
Sun: filaments, prominences
Sun: flares
Sun: fundamental parameters
Sun: general
Sun: granulation
Sun: helioseismology
Sun: heliosphere
Sun: infrared
Sun: interior
Sun: magnetic fields
Sun: oscillations
Sun: particle emission
Sun: photosphere
Sun: radio radiation
Sun: rotation
(Sun:) solar–terrestrial relations
(Sun:) solar wind
(Sun:) sunspots
Sun: transition region
Sun: UV radiation
Sun: X-rays, gamma-rays

Planetary systems

comets: general

comets: individual: . . .

Earth
interplanetary medium
Kuiper belt: general

Kuiper belt objects: individual: . . .

meteorites, meteors, meteoroids

minor planets, asteroids: general

minor planets, asteroids: individual: . . .

Moon
Oort Cloud
planets and satellites: atmospheres
planets and satellites: aurorae
planets and satellites: composition
planets and satellites: detection
planets and satellites: dynamical evolution and stability
planets and satellites: formation
planets and satellites: fundamental parameters
planets and satellites: gaseous planets
planets and satellites: general

planets and satellites: individual: . . .

planets and satellites: interiors
planets and satellites: magnetic fields
planets and satellites: oceans
planets and satellites: physical evolution
planets and satellites: rings
planets and satellites: surfaces
planets and satellites: tectonics
planets and satellites: terrestrial planets
planet–disc interactions
planet–star interactions
protoplanetary discs
zodiacal dust

Stars

stars: abundances
stars: activity
stars: AGB and post-AGB
stars: atmospheres
(stars:) binaries (*including multiple*): close
(stars:) binaries: eclipsing
(stars:) binaries: general
(stars:) binaries: spectroscopic
(stars:) binaries: symbiotic
(stars:) binaries: visual
stars: black holes
(stars:) blue stragglers
(stars:) brown dwarfs
stars: carbon
stars: chemically peculiar
stars: chromospheres
(stars:) circumstellar matter
stars: coronae
stars: distances
stars: dwarf novae
stars: early-type
stars: emission-line, Be
stars: evolution
stars: flare
stars: formation
stars: fundamental parameters
(stars:) gamma-ray burst: general
(stars:) **gamma-ray burst: individual: . . .**
stars: general
(stars:) Hertzsprung–Russell and colour–magnitude diagrams
stars: horizontal branch
stars: imaging
stars: individual: . . .
stars: interiors

stars: jets
stars: kinematics and dynamics
stars: late-type
stars: low-mass
stars: luminosity function, mass function
stars: magnetars
stars: magnetic field
stars: massive
stars: mass-loss
stars: neutron
(stars:) novae, cataclysmic variables
stars: oscillations (*including pulsations*)
stars: peculiar (*except chemically peculiar*)
(stars:) planetary systems
stars: Population II
stars: Population III
stars: pre-main-sequence
stars: protostars
(stars:) pulsars: general
***(stars:)* pulsars: individual: ...**
stars: rotation
stars: solar-type
(stars:) starspots
stars: statistics
(stars:) subdwarfs
(stars:) supergiants
(stars:) supernovae: general
***(stars:)* supernovae: individual: ...**
stars: variables: Cepheids
stars: variables: Scuti
stars: variables: general
stars: variables: RR Lyrae
stars: variables: S Doradus
stars: variables: T Tauri, Herbig Ae/Be
(stars:) white dwarfs
stars: winds, outflows
stars: Wolf-Rayet

Interstellar medium (ISM), nebulae

ISM: abundances
ISM: atoms
ISM: bubbles
ISM: clouds
(ISM:) cosmic rays
(ISM:) dust, extinction
ISM: evolution
ISM: general
(ISM:) HII regions
(ISM:) Herbig–Haro objects

ISM: individual objects: ...
(except planetary nebulae)
ISM: jets and outflows
ISM: kinematics and dynamics
ISM: lines and bands
ISM: magnetic fields
ISM: molecules
(ISM:) photodissociation region (PDR)
(ISM:) planetary nebulae: general
***(ISM:)* planetary nebulae: individual: ...**
ISM: structure
ISM: supernova remnants

The Galaxy

Galaxy: abundances
Galaxy: bulge
Galaxy: centre
Galaxy: disc
Galaxy: evolution
Galaxy: formation
Galaxy: fundamental parameters
Galaxy: general
(Galaxy:) globular clusters: general
***(Galaxy:)* globular clusters: individual: ...**
Galaxy: halo
Galaxy: kinematics and dynamics
(Galaxy:) local interstellar matter
Galaxy: nucleus
(Galaxy:) open clusters and associations: general
***(Galaxy:)* open clusters and associations: individual: ...**
(Galaxy:) solar neighbourhood
Galaxy: stellar content
Galaxy: structure

Galaxies

galaxies: abundances
galaxies: active
galaxies: bar
(galaxies:) BL Lacertae objects: general
***(galaxies:)* BL Lacertae objects: individual: ...**
galaxies: bulges
galaxies: clusters: general

galaxies: clusters: individual: ...

galaxies: clusters: intracluster medium
galaxies: disc
galaxies: distances and redshifts
galaxies: dwarf
galaxies: elliptical and lenticular, cD
galaxies: evolution
galaxies: formation
galaxies: fundamental parameters
galaxies: general
galaxies: groups: general

galaxies: groups: individual: ...

galaxies: haloes
galaxies: high-redshift

galaxies: individual: ...

galaxies: interactions
(galaxies:) intergalactic medium
galaxies: irregular
galaxies: ISM
galaxies: jets
galaxies: kinematics and dynamics
(galaxies:) Local Group
galaxies: luminosity function, mass function
(galaxies:) Magellanic Clouds
galaxies: magnetic fields
galaxies: nuclei
galaxies: peculiar
galaxies: photometry
(galaxies:) quasars: absorption lines
(galaxies:) quasars: emission lines
(galaxies:) quasars: general

(galaxies:) **quasars: individual: . . .**
(galaxies:) quasars: supermassive black holes
galaxies: Seyfert
galaxies: spiral
galaxies: starburst
galaxies: star clusters: general

galaxies: star clusters: individual: . . .
galaxies: star formation
galaxies: statistics
galaxies: stellar content
galaxies: structure

Cosmology

(cosmology:) cosmic background radiation
(cosmology:) cosmological parameters
(cosmology:) dark ages, reionization, first stars
(cosmology:) dark energy
(cosmology:) dark matter
(cosmology:) diffuse radiation
(cosmology:) distance scale
(cosmology:) early Universe
(cosmology:) inflation
(cosmology:) large-scale structure of Universe
cosmology: miscellaneous
cosmology: observations
(cosmology:) primordial nucleosynthesis
cosmology: theory

ultraviolet: general
ultraviolet: ISM
ultraviolet: planetary systems
ultraviolet: stars
X-rays: binaries
X-rays: bursts
X-rays: diffuse background
X-rays: galaxies
X-rays: galaxies: clusters
X-rays: general
X-rays: individual: . . .
X-rays: ISM
X-rays: stars

Transients

(transients:) black hole mergers
(transients:) black hole - neutron star mergers
(transients:) fast radio bursts
(transients:) gamma-ray bursts
(transients:) neutron star mergers
transients: novae
transients: supernovae
transients: tidal disruption events

Resolved and unresolved sources as a function of wavelength

gamma-rays: diffuse background
gamma-rays: galaxies
gamma-rays: galaxies: clusters
gamma-rays: general
gamma-rays: ISM
gamma-rays: stars
infrared: diffuse background
infrared: galaxies
infrared: general
infrared: ISM
infrared: planetary systems
infrared: stars
radio continuum: galaxies
radio continuum: general
radio continuum: ISM
radio continuum: planetary systems
radio continuum: stars
radio continuum: transients
radio lines: galaxies
radio lines: general
radio lines: ISM
radio lines: planetary systems
radio lines: stars
submillimetre: diffuse background
submillimetre: galaxies
submillimetre: general
submillimetre: ISM
submillimetre: planetary systems
submillimetre: stars
ultraviolet: galaxies